Annual Review of Physical Chemistry

Collective Effects in Polariton Chemistry and Photophysics

Wenxiang Ying,[1] M. Elious Mondal,[1] Eric R. Koessler,[1] Sebastian Montillo Vega,[1] and Pengfei Huo[1,2,3]

[1]Department of Chemistry, University of Rochester, Rochester, New York, USA

[2]The Institute of Optics, Hajim School of Engineering, University of Rochester, Rochester, New York, USA

[3]Center for Coherence and Quantum Science, University of Rochester, Rochester, New York, USA; email: pengfei.huo@rochester.edu

Annu. Rev. Phys. Chem. 2026. 77:201–24

First published as a Review in Advance on January 21, 2026

The *Annual Review of Physical Chemistry* is online at physchem.annualreviews.org

https://doi.org/10.1146/annurev-physchem-082624-023219

Keywords

molecular polariton, optical microcavities, collective light–matter coupling, polariton chemistry, vibrational strong coupling

Abstract

Coupling molecules to the quantized radiation field inside an optical cavity creates a set of new photon–matter hybrid states, so-called polaritons. Recent experiments have demonstrated that molecular polaritons can lead to modifications of excited-state dynamics and spectroscopy, photochemistry, and ground-state chemical reactivities. We review the fundamental theory of molecular polaritons under collective light–matter coupling, where many molecules are simultaneously coupled to the cavity mode. Our discussion is based on model systems that effectively capture the essential physics of experiments, allowing one to obtain analytic theories and valuable insights into the microscopic mechanisms in polariton dynamics and spectroscopy, photochemistry, and vibrational strong coupling–modified chemistry.

1. INTRODUCTION

Delocalized excitation: as a result of quantum mechanics superposition, excitations are delocalized among molecules and cavity modes

Strong coupling: $\hbar\Omega_R > (\kappa + \Gamma)/2$

ESC: electronic/excitonic strong coupling

VSC: vibrational strong coupling

Cavity frequency: ω_c

Light–matter coupling strength: g_c

Dark states (DS): degenerate eigenstates of the light–matter interaction Hamiltonian with no optical transition dipole

Coupling molecules to a quantized radiation field inside an optical microcavity (**Figure 1*a***) creates a set of new photon–matter hybrid states. These hybrid polariton states arise from the superposition between molecular states (electronic or vibrational excitation) and the cavity photon Fock states (photonic excitation)—so-called polaritons (1). These polariton states have delocalized excitations among molecules and cavity modes. The formation of polariton states and their subsequent dynamics are considered key to many crucial phenomena, such as the modification of chemical reactivities (1–5) and vibrational energy transfer (6–10), changes in electron transfer (ET) (11–16) and photoinduced charge transfer (17), hot electron cooling dynamics and photoluminescence in nanomaterials (18–21), exciton transport (22–29), and excitation energy transfer (30–32). Therefore, they present a significant opportunity for innovation in material and energy science quantum information platforms. For example, exciton polaritons could be used for analog quantum simulation (33) and quantum computing (34).

There are two main regimes for polariton chemistry. The first is related to electronic (excitonic) strong coupling (ESC) and photochemistry (3, 35, 36), operating under an external laser field to initiate photochemistry. The resulting hybrid electronic/excitonic–photonic states are usually referred as to exciton polaritons. The second is related to vibrational strong coupling (VSC) and the change of ground-state reactivities (37–40), operating under the so-called dark condition without any external laser pumping. The resulting hybrid molecular vibrational–photonic states are usually referred as to vibration polaritons.

Meanwhile, the light–matter hybrid states decay over time due to exciton–phonon coupling (vibrational environment of each molecule) and cavity losses, causing polariton relaxation and decoherence, which have interesting consequences on polariton dynamics and spectra. To take the polariton decay effects into account, a minimal model Hamiltonian that describes polariton formation in the single-excitation subspace is expressed as (1, 41, 42)

$$\hat{\mathcal{H}} = \begin{bmatrix} \hbar\omega_c - i\kappa/2 & \hbar\sqrt{N}g_c \\ \hbar\sqrt{N}g_c & \hbar\omega_0 - i\Gamma/2 \end{bmatrix}, \quad 1.$$

where ω_c is the cavity frequency, ω_0 is the exciton frequency, g_c is the single-molecule light–matter coupling strength, N is the number of molecules coupled to the cavity, κ is the cavity loss rate, and Γ is the exciton broadening. There are also $N - 1$ dark states (DS) (see Equation 10), which do

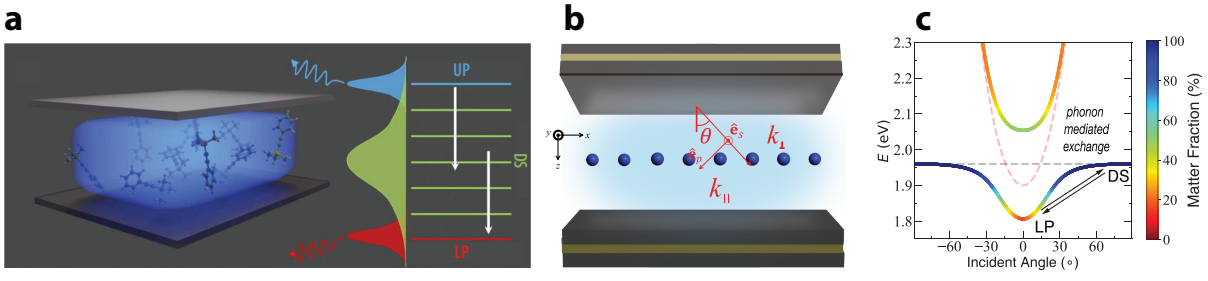

Figure 1

Schematics of collective light–matter coupling inside a Fabry–Pérot cavity. (*a*) Schematic of molecules collectively coupled inside the cavity, forming upper polariton (UP) states, dark states (DS), and lower polariton (LP) states. (*b*) A simplified model of exciton sites coupled to photonic modes with $k_\parallel$. (*c*) Polariton dispersion relation, generated from the hybridization of the photonic dispersion (*pink dashed line*) and excitonic dispersion (*black dashed line*). The polariton dispersion is color-coded according to its photonic character, with red for pure photonic character and blue for pure excitonic character. Panels *b* and *c* reprinted with permission from Reference 29 (CC BY-NC-ND 4.0).

not have photonic character and are not included in Equation 1. Furthermore, the description of polariton decay that adds an imaginary term is phenomenological and has certain limitations. For example, it fails to account for polaritonic effects that arise from the polaron decoupling effect (see Section 2.4) due to a lack of molecular vibrations. One can obtain a microscopic description for molecular polaritons by using the Holstein–Tavis–Cummings (HTC) Hamiltonian (see Section 2.1), which is more complete and does not miss important physics.

Under the resonant condition ($\omega_c = \omega_0$), diagonalizing the Hamiltonian in Equation 1 leads to the following complex eigenvalues (41–43): $E_\pm = \hbar(\omega_0 + \omega_c)/2 - i(\kappa + \Gamma)/4 \pm \sqrt{N\hbar^2 g_c^2 - (\kappa - \Gamma)^2/16}$, where E_+ and E_- are for the upper polariton (UP) and the lower polariton (LP), respectively, whose real part corresponds to the energy of the polariton states and whose imaginary part corresponds to the broadening (or width of the spectral peak). The energy difference between these polariton states is the Rabi splitting, $\hbar\Omega_R = E_+ - E_-$. The strong coupling condition is typically defined as $\hbar\Omega_R > (\kappa + \Gamma)/2$, such that one can observe the splitting of the peaks in spectral measurements. Recent theoretical research (44) suggests that, in the presence of energy disorder (molecular transitions occur at different frequencies as a result of their local environments), delocalization of polariton states requires the collective light–matter coupling strength $\hbar\sqrt{N}g_c$ to exceed four times the standard deviation of the energy disorder line width, in addition to simply observing the Rabi splitting. Most experiments operate under the collective light–matter coupling regime, where the cavity mode interacts simultaneously with a large ensemble of molecules ($N \gg 1$), giving rise to a sizable Rabi splitting, $\hbar\Omega_R \propto \hbar\sqrt{N}g_c$. Typical values of N have been estimated to be in the range of $N \approx 10^3$–10^6 per cavity mode for ESC (18, 21) and $N \approx 10^6$–10^{12} per cavity mode for VSC (45). In experiments, the Rabi splitting is often in the range of $\hbar\Omega_R \approx 50$–420 meV for ESC (18) and $\hbar\Omega_R \approx 38$–180 cm^{-1} for VSC (37, 40, 46). For matter optical transition frequency, typical values are $\hbar\omega_0 \approx 2$ eV for ESC and $\hbar\omega_0 \approx 800$–$3{,}600$ cm^{-1} for VSC.

How this collective light–matter coupling strength $\hbar\sqrt{N}g_c$ affects optical properties (e.g., polariton linear absorption spectra) is well-understood. However, how it affects polariton photochemistry (5) and VSC chemistry (47, 48) remains elusive, and there are no well-accepted mechanisms. Many open questions have yet to be resolved, including the following:

1. How can a weak coupling strength per molecule g_c change chemistry and lead to collective effects?
2. How can delocalized excitations among molecules and cavity modes influence local chemical reactions (e.g., the intrinsic reaction mechanism of a single molecule in the absence of a cavity)?
3. How does the dense manifold of dark exciton states influence polariton chemistry?

Intuitively, one may expect the collective quantity $\hbar\Omega_R$ to manifest in the rate constant of these reactions when coupled to the cavity.

This review summarizes collective effects in polariton chemistry and photophysics arising from the nature of collective light–matter coupling and addresses many controversies in this field (both experimental and theoretical). In Section 2, we provide a theoretical overview of collective light–matter interaction Hamiltonians, with diabatic or adiabatic representations of polariton states, and introduce the polaron decoupling effect. In Section 3, we discuss some simple rate theories for polariton relaxation dynamics, decoherence, and linear spectra lineshape. In Section 4, we present a collective mechanism for the rate enhancement of polariton-mediated electron transfer (PMET) reactions. In Section 5, we discuss recent theoretical developments that provide insights into the resonant rate suppression effects in VSC.

UP: upper polariton

LP: lower polariton

Rabi splitting: $\hbar\Omega_R \propto \sqrt{N}g_c$

Collective light–matter coupling: the cavity mode interacts simultaneously with a large ensemble of molecules ($N \gg 1$)

PMET: polariton-mediated electron transfer

2. THEORETICAL MODELS

Molecular excitation frequency: ω_0

In typical experiments, molecule ensembles are collectively coupled to many cavity modes (**Figure 1*b***) that satisfy a certain dispersion relation (**Figure 1*c***). For Fabry–Pérot cavities (see schematics in **Figure 1*a***) with refractive index n_c, the dispersion is

$$\hbar\omega_{\mathbf{k}}(k_\parallel) = \frac{\hbar c}{n_c}\sqrt{k_\perp^2 + k_\parallel^2} = \frac{\hbar c}{n_c}k_\perp\sqrt{1+\tan^2\theta}, \qquad 2.$$

where c is the speed of light, $\hbar k_\parallel$ is the in-plane photonic momentum, and $\hbar k_\perp$ is the photonic momentum along the quantized direction. The angle θ indicates the direction of $\mathbf{k}$ relative to the normal direction of the cavity mirror (**Figure 1*b***). When $k_\parallel = 0$, the photon frequency is $\hbar\omega_c \equiv \hbar\omega_{\mathbf{k}}(k_\parallel = 0) = \hbar c k_\perp / n_c$.

A general model Hamiltonian that describes N noninteracting, identical, two-level excitons coupled to many cavity modes (Equation 2) can be expressed as (1)

$$\hat{H} = \sum_{n=1}^{N}\hbar\omega_0\hat{\sigma}_n^+\hat{\sigma}_n^- + \sum_{\mathbf{k}}\hbar\omega_{\mathbf{k}}\left(\hat{a}_{\mathbf{k}}^\dagger\hat{a}_{\mathbf{k}} + \frac{1}{2}\right) + \sum_{n=1}^{N}\sum_{\mathbf{k}}\hbar g_{n\mathbf{k}}\left(\hat{a}_{\mathbf{k}}^\dagger\hat{\sigma}_n^- e^{-i\mathbf{k}\cdot\mathbf{r}_n} + \hat{a}_{\mathbf{k}}\hat{\sigma}_n^+ e^{i\mathbf{k}\cdot\mathbf{r}_n}\right), \qquad 3.$$

where we ignore the dipole self-energy and assume the rotating-wave approximation (1) (ignoring terms such as $\hat{a}^\dagger\hat{\sigma}_n^+$ and $\hat{a}\hat{\sigma}_n^-$ that do not conserve excitation). In Equation 3, $\hat{\sigma}_n^+ = |e_n\rangle\langle g_n|$ ($\hat{\sigma}_n^- = |g_n\rangle\langle e_n|$) is the creation (annihilation) operator of the nth exciton, whose ground and excited states are $|g_n\rangle$ and $|e_n\rangle$, respectively, with a molecular excitation frequency of ω_0 (for the $|g_n\rangle \rightarrow |e_n\rangle$ transition). The position of the nth exciton is $\mathbf{r}_n$. The transition dipole operator is $\hat{\boldsymbol{\mu}}_n = \boldsymbol{\mu}_{eg}(\hat{\sigma}_n^+ + \hat{\sigma}_n^-)$, assuming that all excitons have the same dipole moment. Furthermore, $\hat{a}_{\mathbf{k}}$ and $\hat{a}_{\mathbf{k}}^\dagger$ are the photonic field annihilation and creation operators for mode $\mathbf{k}$, whose frequency is $\omega_{\mathbf{k}}$. The anisotropic light–matter coupling strength is $g_{n\mathbf{k}}$. A detailed derivation of the Hamiltonian in Equation 3 can be found in Reference 1.

On the basis of Equation 3, one can obtain a simplified description by setting $\mathbf{r}_n = 0$ for all excitons n when the molecular system size is much smaller than $c/(2\pi\omega_0)$, known as the long-wavelength approximation (1). Furthermore, by taking a single radiation field mode as a cavity mode and assuming a uniform coupling strength $g_{n\mathbf{k}} = g_c$, one can arrive at the celebrated Tavis–Cummings (TC) model (49, 50) (see Equation 4, below), which is a minimal theoretical model describing collective light–matter coupling. The TC Hamiltonian can be analytically diagonalized in the single-excitation subspace, leading to two polariton states and $N - 1$ DS (see Section 2.2).

Next, one accounts for polariton relaxation and decoherence (which are important in chemistry and photophysics) by incorporating molecular vibrations (phonons) and exciton–phonon couplings into the TC model, leading to the HTC model (1, 18, 51–53) (see Section 2.1, below). The HTC model has been widely used in the study of exciton polaritons in molecular aggregates (51, 52, 54) as well as in polariton condensation and lasing (55, 56), in which the exciton–phonon couplings are included in the Hamiltonian via a system-bath model (57) that corresponds to a microscopic description of molecular dissipation and contrasts with the oversimplified non-Hermitian effective Hamiltonian in Equation 1. We focus on the HTC type of Hamiltonian throughout this review; the details depend on the problem studied [i.e., more complicated reaction coordinates are considered when studying polariton-modified chemistry (PMET and VSC)].

2.1. The Holstein–Tavis–Cummings Hamiltonian

We consider the single-mode HTC Hamiltonian expressed in the form of a system-bath model (57) as $\hat{H}_{\mathrm{HTC}} = \hat{H}_{\mathrm{S}} + \hat{H}_{\mathrm{B}} + \hat{H}_{\mathrm{SB}} + \hat{H}_{\mathrm{loss}}$.

2.1.1. Molecule–cavity interactions. The system term $\hat{H}_S$ consists of the excitonic degree of freedom (DOF) of the molecules and the photonic DOF of the cavity,

$$\hat{H}_S = \sum_{n=1}^{N} \hbar\omega_0 \hat{\sigma}_n^+ \hat{\sigma}_n^- + \hbar\omega_c \left(\hat{a}^\dagger \hat{a} + \frac{1}{2}\right) + \hbar g_c \sum_{n=1}^{N} \left(\hat{a}^\dagger \hat{\sigma}_n^- + \hat{a}\hat{\sigma}_n^+\right), \quad 4.$$

which is the TC Hamiltonian (49, 50). The second term in Equation 4 describes a cavity mode of frequency ω_c, and the third term is the light–matter (exciton–photon) interaction. The light–matter coupling strength is $g_c = \sqrt{\omega_c/(2\hbar\epsilon\mathcal{V})}\ \hat{\mathbf{e}} \cdot \boldsymbol{\mu}_{eg}$, where $\hat{\mathbf{e}}$ is the cavity field polarization direction, ϵ is the permittivity inside the cavity (for vacuum, $\epsilon = \epsilon_0$), and $\mathcal{V}$ is the effective cavity quantization volume. In Equation 4, we assume identical excitons with no inhomogeneous energy or orientational dipole disorder.

Reorganization energy: λ

Cavity lifetime: τ_c

Cavity loss rate: $\kappa/\hbar \equiv \tau_c^{-1}$

Cavity quality factor: $\mathcal{Q} = \omega_c \tau_c$

Detuning: $\Delta_\omega = \omega_c - \omega_0$

2.1.2. System-bath Hamiltonian. The bath Hamiltonian is $\hat{H}_B = \sum_{\alpha,n} \hbar\omega_\alpha \hat{b}_{\alpha,n}^\dagger \hat{b}_{\alpha,n}$, where $\hat{b}_{\alpha,n}$ ($\hat{b}_{\alpha,n}^\dagger$) is the annihilation (creation) operator for the αth phonon mode on the nth exciton of frequency ω_α. Furthermore, the excitons interact with the phonons according to the Holstein-like interaction $\hat{H}_{SB} = \sum_n \hat{\sigma}_n^+ \hat{\sigma}_n^- \otimes \sum_\alpha c_\alpha (\hat{b}_{\alpha,n} + \hat{b}_{\alpha,n}^\dagger)$, where c_α is the coupling strength of the αth phonon with the nth exciton, sampled from a spectral density $J_n(\omega) = J(\omega) = (\pi/\hbar) \sum_\alpha c_\alpha^2 \delta(\omega - \omega_\alpha)$, where $\lambda = (1/\pi) \int_0^{+\infty} d\omega\, J(\omega)/\omega = \sum_\alpha c_\alpha^2/(\hbar\omega_\alpha)$ is the reorganization energy. For model parameterization, atomistic simulations of real molecular systems can be used to construct $J(\omega)$ and obtain λ (58).

2.1.3. Cavity loss dynamics. The cavity lifetime τ_c is finite because of its coupling to the far-field photon modes outside the cavity, described by the Hamiltonian $\hat{H}_{loss} = \sum_k \hbar\omega_k \hat{b}_k^\dagger \hat{b}_k + (\hat{a}^\dagger + \hat{a}) \otimes \sum_k \hbar g_k (\hat{b}_k^\dagger + \hat{b}_k)$, where $\hat{b}_k^\dagger$ ($\hat{b}_k$) is the raising (lowering) operator for the kth far-field mode. The interactions between the cavity mode and the far-field modes can be described by the Gardiner–Collett interaction Hamiltonian (59–61), where the broad range of the far-field frequencies leads to a short correlation time, justifying the Markovian treatment of loss and giving rise to the Lindblad master equation (62), $d\hat{\rho}_S/dt = -(i/\hbar)[\hat{H}_S, \hat{\rho}_S] + (\kappa/\hbar)[\hat{a}\hat{\rho}_S\hat{a}^\dagger - (1/2)\{\hat{a}^\dagger\hat{a}, \hat{\rho}_S\}]$. Here, $\hat{\rho}_S$ is the reduced density matrix associated with $\hat{H}_S$ and $\kappa/\hbar \equiv \tau_c^{-1}$ is the cavity loss rate, which is experimentally related to the cavity quality factor $\mathcal{Q} = \omega_c \tau_c$.

2.2. Polariton States and Dark States

For the Hamiltonian in Equation 4, the ground state is $|G, 0\rangle = |g_1\rangle \otimes \ldots \otimes |g_N\rangle \otimes |0\rangle$ and the first excitation subspace is spanned by

$$|G, 1\rangle = |g_1\rangle \otimes \ldots \otimes |g_N\rangle \otimes |1\rangle, \quad |E_n, 0\rangle = |g_1\rangle \otimes \ldots |e_n\rangle \ldots \otimes |g_N\rangle \otimes |0\rangle, \quad 5.$$

where $|0\rangle$ and $|1\rangle$ are the vacuum and one-photon Fock states, respectively. One can define a collective bright excitonic state $|B, 0\rangle = (1/\sqrt{N}) \sum_{n=1}^{N} |E_n, 0\rangle$, which carries the optical transition dipole from the ground state, $\langle G, 0|\hat{\mu}|B, 0\rangle = \sum_{n=1}^{N} (\mu_{eg}/\sqrt{N}) = \sqrt{N}\mu_{eg}$. Note that we have assumed that the dipoles are all aligned to the cavity field polarization, so that $\hat{\mathbf{e}} \cdot \boldsymbol{\mu}_{eg} = \mu_{eg}$. The light–matter interactions hybridize $|B, 0\rangle$ and $|G, 1\rangle$, leading to two bright polariton eigenstates (of $\hat{H}_S$),

$$|+\rangle = \cos\Theta \cdot |B, 0\rangle + \sin\Theta \cdot |G, 1\rangle, \quad |-\rangle = -\sin\Theta \cdot |B, 0\rangle + \cos\Theta \cdot |G, 1\rangle, \quad 6.$$

where the mixing angle is $\Theta = (1/2)\tan^{-1}[2\sqrt{N}g_c/(\Delta_\omega)]$, with $\Theta \in [0, \pi/2)$, and the light–matter detuning is $\Delta_\omega \equiv \omega_c - \omega_0$. At resonance, $\Delta_\omega = 0$ and $\Theta = \pi/4$. Note that Θ can also be expressed in terms of the Hopfield coefficients (1, 43, 63),

$$|C|^2 = \sin^2\Theta = \frac{1}{2}\left[1 + \frac{\Delta_\omega}{\sqrt{\Delta_\omega^2 + 4Ng_c^2}}\right], \quad |X|^2 = \cos^2\Theta = \frac{1}{2}\left[1 - \frac{\Delta_\omega}{\sqrt{\Delta_\omega^2 + 4Ng_c^2}}\right]. \quad 7.$$

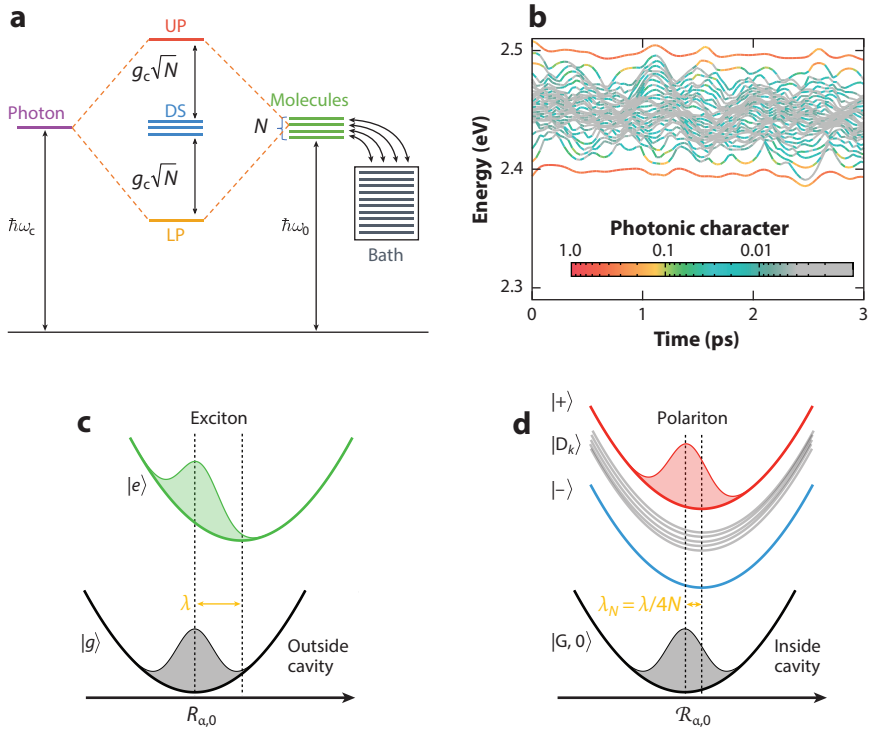

Figure 2

Schematic of N excitons collectively coupled to a cavity mode, forming $N + 1$ eigenstates [upper polariton (UP), lower polariton (LP), and dark states (DS)], under (*a*) the diabatic representation and (*b*) the adiabatic representation. (*c*) The ground-state $|g\rangle$ potential energy surface (PES) (*gray*) and excited-state $|e\rangle$ PES (*green*) with a Frank–Condon excited wave packet when a bare molecular exciton is presented outside the cavity. (*d*) The collective ground state $|G, 0\rangle$ PES (*gray*) and UP $|+\rangle$ PES (*red*) with a Frank–Condon excited wave packet when N molecules collectively couple to a cavity mode. The LP $|-\rangle$ PES (*blue*) and the DS $|D_k\rangle$ PES (*dark gray*) are also depicted. Panel *a* adapted with permission from Reference 65. Panel *b* adapted with permission from Reference 18.

The corresponding eigenfrequencies are expressed as

$$\omega_\pm = \frac{1}{2}(\omega_0 + \omega_c) \pm \frac{1}{2}\sqrt{\Delta_\omega^2 + 4Ng_c^2} \qquad 8.$$

and are depicted schematically in **Figure 2*a***.

The Rabi splitting is a collective quantity and is defined as

$$\hbar\Omega_R = \hbar\omega_+ - \hbar\omega_- = \hbar\sqrt{\Delta_\omega^2 + 4Ng_c^2}. \qquad 9.$$

At resonance ($\Delta_\omega = 0$), Equation 9 becomes $\Omega_R = 2\sqrt{N}g_c$, which makes $\hbar\Omega_R$ a collective quantity. Experimentally, even a small g_c can result in a large $\hbar\Omega_R$ due to very large N.

Apart from the two polariton eigenstates in Equation 6, $\hat{H}_S$ has additional $N - 1$ degenerate eigenstates in the first excitation manifold (Equation 5), with eigenenergies $\hbar\omega_0$, that are commonly expressed in the delocalized Fourier basis (1, 49, 64):

$$|D_k\rangle = \frac{1}{\sqrt{N}}\sum_{n=1}^{N}\exp\left(-2\pi i\frac{nk}{N}\right)|E_n, 0\rangle, \qquad 10.$$

where $k \in \{1, \ldots, N-1\}$. These are commonly referred to as DS because of their optically dark nature: $\langle \mathrm{G}, 0|\hat{\mu}|\mathrm{D}_k\rangle = (\mu_{eg}/\sqrt{N}) \cdot \sum_{n=1}^{N} \exp[-2\pi i\,(nk/N)] = 0$.

Under the polariton basis, the TC Hamiltonian becomes purely diagonal: $\hat{H}_{\mathrm{S}} = \hbar\omega_+|+\rangle\langle+| + \hbar\omega_-|-\rangle\langle-| + \hbar\omega_0 \sum_{k=1}^{N-1} |\mathrm{D}_k\rangle\langle\mathrm{D}_k|$. Through the use of discrete Fourier transform for the phonon operators, $\hat{b}_{\alpha,k} = (1/\sqrt{N}) \sum_{n=1}^{N} \exp[2\pi i(nk/N)]\hat{b}_{\alpha,n}$, the bath Hamiltonian is $\hat{b}_{\mathrm{B}} = \sum_{\alpha,k} \hbar\omega_\alpha \hat{b}^\dagger_{\alpha,k}\hat{b}_{\alpha,k}$, and the system-bath Hamiltonian becomes (65, 66)

$$\hat{H}_{\mathrm{SB}} = \sum_{\eta\nu,kk'} \xi_{\eta k} \cdot \xi_{\nu k'} |\eta_k\rangle\langle\nu_{k'}| \otimes \sum_{\alpha} \frac{c_\alpha}{\sqrt{N}} (\hat{b}_{\alpha,k-k'} + \hat{b}^\dagger_{\alpha,k'-k}), \qquad 11.$$

where the state labels $\eta, \nu \in \{+, -\}$ for $k = 0$ (bright) and $\eta, \nu \equiv \mathrm{D}$ for $k \neq 0$ (dark). Furthermore, $\xi_{\eta k}$ is a state-dependent coefficient that characterizes the matter fraction of the polariton state, with $\xi_+ = \cos\Theta$ and $\xi_- = \sin\Theta$ for $k = 0$ and $\xi_{\mathrm{D}k} = 1$ for $k \neq 0$. Note that $|\xi_\pm|^2$ are simply the Hopfield coefficients in Equation 7. Equation 11 shows that transitions between eigenstates are mediated by phonons. In particular, $\langle \mathrm{D}_k|\hat{H}_{\mathrm{SB}}|+\rangle = \cos\Theta \cdot \sum_\alpha (c_\alpha/\sqrt{N})(\hat{b}_{\alpha,k} + \hat{b}^\dagger_{\alpha,-k})$ and $\langle \mathrm{D}_k|\hat{H}_{\mathrm{SB}}|-\rangle = \sin\Theta \cdot \sum_\alpha (c_\alpha/\sqrt{N})(\hat{b}_{\alpha,-k} + \hat{b}^\dagger_{\alpha,k})$ cause $|\pm\rangle \leftrightarrow |\mathrm{D}_k\rangle$ transitions.

2.3. Diabatic Versus Adiabatic Representations of Polariton States

The polariton states and DS in Equations 6 and 10 are defined in the absence of nuclear motion, as they are constructed from the photonic and electronic DOFs with the nuclear configuration held fixed (i.e., independently of $\{\hat{R}_{n,\alpha}\}$ or $\hat{b}^\dagger_{\alpha,n} + \hat{b}_{\alpha,n}$). These are often referred to as the diabatic polariton states because they do not account for the dependence of polaritonic eigenstates on the nuclear coordinates. In this representation, the nuclear DOFs act as a bath, leading to transitions between polariton states and DS through exciton–phonon interactions (see $\hat{H}_{\mathrm{SB}}$ in Equation 11).

Alternatively, one can define the adiabatic polariton representation by treating the nuclear coordinates as parameters and diagonalizing the full electronic–photonic Hamiltonian at each fixed nuclear geometry $\mathbf{R} = \{R_{n,\alpha}\}$ (i.e., $\hat{H}_{\mathrm{pl}} = \hat{H} - \hat{T}_R$, excluding nuclear kinetic energy) and solving $\hat{H}_{\mathrm{pl}}(\mathbf{R})|\Phi_k(\mathbf{R})\rangle = E_k(\mathbf{R})|\Phi_k(\mathbf{R})\rangle$. The resulting eigenstates $|\Phi_k(\mathbf{R})\rangle$ then include the influence of the nuclear environment, and the nuclear dynamics occurs on the polariton potential energy surfaces (PESs) (for an example, see **Figure 2*b***). In this picture, nonadiabatic couplings [also known as derivative couplings, i.e., terms such as $\langle\Phi_i(\mathbf{R})|\nabla_{n,\alpha}|\Phi_j(\mathbf{R})\rangle$ that originate from the bath nuclear momentum operator $\hat{P}_{n,\alpha} = -i\hbar\nabla_{n,\alpha}$] govern the transitions between adiabatic polariton states and are responsible for energy transfer, decoherence, and relaxation.

The choice between these representations depends on the physical situation of interest. The diabatic picture is particularly convenient for describing transitions mediated by phonon baths [e.g., using quantum master equation approaches (65, 66)], while the adiabatic picture is useful for describing nuclear wave-packet dynamics (67–69) or semiclassical propagation (68–70) with nonadiabatic transitions. Importantly, these adiabatic DS are no longer degenerate and no longer strictly dark (18), as their character depends on the local nuclear configurations $\mathbf{R} = \{R_{n,\alpha}\}$ (**Figure 2*b***). This lifting of degeneracy is crucial for understanding decoherence and energy flow between bright and dark manifolds.

2.4. Polaron Decoupling Effect

Herrera & Spano (51, 52) demonstrated that a strong collective resonant coupling of a cavity field with N exciton transitions effectively decouples polaritons from phonon interactions, as confirmed experimentally (71). Specifically, the (diagonal) exciton–phonon coupling strength c_α is rescaled as $c_\alpha/\sqrt{N}$ for both the diagonal (Holstein coupling) and off-diagonal (Peierls coupling) polariton-phonon coupling terms associated with the bright states $|\pm\rangle$ (see Equation 11). As such,

the relative displacement caused by the αth phonon on the $|\pm\rangle$ state with respect to $|G, 0\rangle$ is given by (52) $\mathcal{R}_{\alpha,0} = R_{\alpha,0}/(2\sqrt{N})$ (at resonance), where $R_{\alpha,0} = \sqrt{2c_\alpha^2/(M_\alpha \hbar \omega_\alpha^3)}$ (with reduced mass $M_\alpha = 1$ atomic unit). Thus, the effective reorganization energy for the $|\pm\rangle$ state becomes

$$\lambda_N = \frac{1}{2}\sum_\alpha M_\alpha \omega_\alpha^2 \mathcal{R}_{\alpha,0}^2 = \frac{\lambda}{4N}, \tag{12.}$$

which is $4N$ times smaller than outside the cavity. When the Rabi oscillation period is shorter than vibrational timescales, excitons can exchange energy with the cavity mode multiple times before nuclei adapt to the excited-state potential. For large N, the homogeneous reorganization energy approaches zero, so the equilibrium positions of the bright and ground-state potentials align (51, 52). Using the shifted harmonic oscillator model (72), **Figure 2*c*** illustrates the PESs for both the ground ($|g\rangle$) and excited ($|e\rangle$) states of an isolated molecular exciton. The ground-state PES features a thermal wave packet at equilibrium, which, when subjected to Franck–Condon (FC) excitation, causes the wave packet to shift within the excited state relative to the minima of its corresponding PES. Similarly, **Figure 2*d*** depicts the effect of polaron decoupling. The polaritonic states, $|+\rangle$ and $|-\rangle$, remain largely unshifted relative to the ground state, causing the FC excited-state wave packet to closely resemble the ground-state thermal wave packet and also significantly reducing the nonadiabatic force arising from an excited-state PES shift (as observed for excitons) in wave-packet dynamics.

3. EXCITON POLARITON RELAXATION DYNAMICS AND SPECTRA

In this section, we review several analytic results derived from the HTC Hamiltonian that shed light on the fundamental properties of molecular polaritons under the collective coupling regime. A broad spectrum of experimental studies on the excited-state properties of exciton polaritons have been conducted (73–81). Most of these experimental results are well-understood on the basis of the current theoretical framework.

3.1. Polariton Relaxation Dynamics

Computational studies of the HTC model excited-state properties used various exact quantum dynamics methods (82–85) and trajectory-based mixed quantum–classical methods (86, 87). Exploiting the symmetry and sparsity of $\hat{H}_S$ can notably lower the scaling and computational costs for $(\hat{H}_S + \hat{H}_{SB})|\Psi(t)\rangle$, allowing direct simulations of the HTC model with $N = 10^6$ (for details, see 87). Exploiting the symmetry of the HTC Hamiltonian can bypass the need to explicitly simulate dynamics with large N. For example, by assuming uncorrelated excitons, one can represent the dynamics with a pair of mean-field equations of motion (88, 89) for one excitonic and one photonic DOF. Another example is the CUT-E (collective dynamics using truncated equations) approach (90), which leverages the permutational symmetry of matter states to reduce computational demands through an effective $1/N$ expansion (91).

In contrast, the polariton relaxation dynamics can be well-described by Fermi's golden rule (FGR) rate constants when the phonon bath coupling $\hat{H}_{SB}$ can be treated perturbatively (65). In particular, the $|\pm\rangle \rightarrow \{|D_k\rangle\}$ transition rates are (65, 92)

$$k_{+\rightarrow D} = \frac{N-1}{\hbar N}\cdot(1+\cos 2\Theta)\cdot J(\omega_+ - \omega_0)\cdot[\overline{n}(\omega_+ - \omega_0)+1], \tag{13a.}$$

$$k_{-\rightarrow D} = \frac{N-1}{\hbar N}\cdot(1-\cos 2\Theta)\cdot J(\omega_0 - \omega_-)\cdot \overline{n}(\omega_0 - \omega_-), \tag{13b.}$$

where $\bar{n}(\omega) = 1/(e^{\beta\hbar\omega} - 1)$ is the Bose–Einstein distribution function, $\beta = 1/(k_B T)$ is the inverse temperature, and k_B is the Boltzmann constant. Starting from an arbitrary state in the DS manifold (or even a statistical mixture of them), we find that the $\{|D_k\rangle\} \to |-\rangle$ transition rate is

$$k_{D\to-} = \frac{1}{\hbar N} \cdot (1 - \cos 2\Theta) \cdot J(\omega_0 - \omega_-) \cdot \bar{n}(\omega_0 - \omega_-). \quad 13c.$$

Bose–Einstein distribution function: $\bar{n}(\omega) = 1/(e^{\beta\hbar\omega} - 1)$

Inverse temperature: $\beta = 1/(k_B T)$

Thus, unlike $k_{\pm\to D}$ (Equations 13*a* and *b*), $k_{D\to-}$ does not include the $N - 1$ degeneracy factor. The reason is that $|\pm\rangle \to \{|D_k\rangle\}$ involves $N - 1$ degenerate final states, whereas $\{|D_k\rangle\} \to |-\rangle$ involves only $|-\rangle$ as the final state and does not acquire the $N - 1$ factor. Thus, $\{|D_k\rangle\} \to |-\rangle$ occurs much more slowly than $|\pm\rangle \to \{|D_k\rangle\}$. In real experiments (6, 7), dark excitons also decay via nonradiative relaxation, but the timescale is much longer than the polariton lifetime. Furthermore, the large $N - 1$ degeneracy of the DS manifold may be interpreted from the entropy perspective (93), because Equation 13*b* can be recast as $k_{-\to D} \approx (1/\hbar N) \cdot [1 - \cos(2\Theta)] \cdot J(\omega_0 - \omega_-) \cdot e^{-\beta\left[\hbar(\omega_0-\omega_-) - k_B T \ln(N-1)\right]}$, such that one can define an effective entropy change $\Delta S = k_B \ln(N - 1)$ associated with the transition. Note that the effective entropy change ΔS differs from the thermodynamics entropy because $N - 1$ is not the actual particle number but rather the degeneracy fold of the DS manifold. When the DS dominate the equilibrium population, the effective entropy change can be explained as the DS manifold having a relatively lower free energy than the LP, with $\Delta\mathcal{F} = \hbar(\omega_0 - \omega_-) - k_B T \ln(N - 1) \equiv \Delta E - T\Delta S < 0$.

Note that the FGR expressions in Equations 13*a–c* are based on an equilibrium assumption and ignore any transient nonequilibrium dynamics. One can derive a nonequilibrium version of these FGR rates using the quantum time-correlation function formalism (65) that are time dependent and, upon taking the long-time limit, reduce to the equilibrium FGR rate constants. These simple FGR rate constants in Equations 13*a–c* offer insight into why simulating polariton relaxation dynamics with a reduced N and elevated g_c often succeeds, provided that the Rabi splitting $\hbar\Omega_R \propto \hbar\sqrt{N} g_c$ stays constant. The key is that the relaxation rates in Equations 13*a–c* are influenced by collective quantities (Ω_R and N) instead of the individual coupling strength g_c.

3.2. Polariton Coherence Decay

The polaron decoupling effect (51, 87, 94, 95) discussed in Section 2.4 can protect overall quantum coherence from phonon coupling–induced decoherence, for both the single-molecule strong coupling regime (96) and the collective coupling regime (87, 92, 97). This effect was confirmed with a prolonged beating off-diagonal signal in two-dimensional electronic spectroscopy (98). Compared with the typical electronic coherence lifetime ($T_2 \sim 15$ fs), the coherence lifetime of exciton polaritons can be extended to ~100 fs at room temperature (92).

The polaritonic coherence can be characterized by the amplitude of $\rho_{+-}(t) = \langle +|\hat{\rho}_S(t)|-\rangle$. Reference 92 shows that the primary decoherence mechanism is the population transfer from the bright state to the DS manifold as well as the cavity loss. Increasing Ω_R prolongs the coherence lifetime as a result of the phonon bottleneck effect (19). Under the $N \to \infty$ condition, transitions between bright polariton states are negligible. As such, the polariton coherence lifetime can be approximated as (92)

$$T_2^{-1} \approx \frac{1}{2} k_{+\to D} + \frac{1}{2} k_{-\to D} + \frac{1}{2} \tau_c^{-1}, \quad 14.$$

where $k_{\pm\to D}$ is expressed in Equations 13*a* and *b* and τ_c^{-1} is the cavity loss rate. For $\Delta_\omega \leqslant 0$, the rate $k_{-\to D}$ can be ignored because of the uphill $|-\rangle \to \{|D_k\rangle\}$ transition. For $\Delta_\omega > 0$, the LP is closer to the DS manifold than the UP, and both $k_{\pm\to D}$ could have significant contributions. Equation 14 predicts the fundamental scaling relation between T_2^{-1} with respect to N, $\sqrt{N} g_c$,

Drude–Lorentz spectral density: $J(\omega) = (2\lambda\gamma\omega)/(\omega^2 + \gamma^2)$

Characteristic frequency: γ

τ_c, and Δ_ω. For example, when $J(\omega)$ takes a Drude–Lorentz form [$J(\omega) = (2\lambda\gamma\omega)/(\omega^2 + \gamma^2)$, where λ is the reorganization energy and γ is the characteristic frequency], Equation 14 suggests that $T_2^{-1} \propto (N-1)/(N^{3/2}g_c)$, which has been confirmed by numerical exact quantum dynamics simulations using the hierarchical equations of motion (HEOM) approach (92). Furthermore, Equation 14 predicts that a turnover of T_2 will occur as one changes the Δ_ω values (92). These predictions can be experimentally verified with state-of-the-art two-dimensional electronic spectroscopy measurements (98) that directly report off-diagonal beatings between the UP and LP states. The prolonged polariton coherence at room temperature could be useful for quantum information science applications (33, 34).

3.3. Polariton Linear Absorption Spectra

Linear absorption spectra can be directly computed from the Fourier transform of the dipole–dipole correlation function according to $\mathcal{A}(\omega) \propto \int_0^\infty dt\, \mathcal{A}(t)e^{i\omega t}$, where $\mathcal{A}(t) \equiv \mathrm{Tr}\left[\hat{\mu}(t)\hat{\mu}(0)\hat{\rho}_g\right]$ and $\hat{\rho}_g$ is the ground-state reduced density matrix for the system (72, 99). **Figure 3*a*** presents $\mathcal{A}(t)$ and $\mathcal{A}(\omega)$ for $\Delta_\omega = 0$ at different values of Ω_R by increasing N, simulated using nonadiabatic partial linearized density matrix dynamics (87). The figure shows that $\mathcal{A}(t)$ oscillates with the frequency of $|G, 0\rangle \rightarrow |\pm\rangle$ transitions and an overall envelope beating related to Ω_R. Increasing Ω_R by raising N causes $\mathcal{A}(t)$ to oscillate faster and longer because of the reduction of λ_N (Equation 12) from the polaron decoupling effect.

In contrast, with a phenomenological description of the molecular dissipation (see Equation 1) and under the $N \rightarrow \infty$ limit, Reference 100 derived an analytic expression for the polariton lineshape as follows: $\mathcal{A}(\omega) = \kappa\Gamma N g_c^2 / \left|[\omega - \omega_c + i(\Gamma/2\hbar)][\omega - \omega_0 + i(\kappa/2\hbar)] - N g_c^2\right|^2$ (see equation 38b of Reference 100). This expression is closely connected to the transfer matrix method (101) and, in turn, yields the polariton line width $\Gamma_\pm = -2\Im\mathcal{A}(\omega_\pm)$, expressed as

$$\Gamma_- = |X|^2\kappa + |C|^2\Gamma, \quad \Gamma_+ = |C|^2\kappa + |X|^2\Gamma, \qquad 15.$$

which is the sum of the cavity and exciton broadening weighted by their Hopfield coefficients (43). However, Equation 15 does not capture the subaverage behavior of the polariton line width,

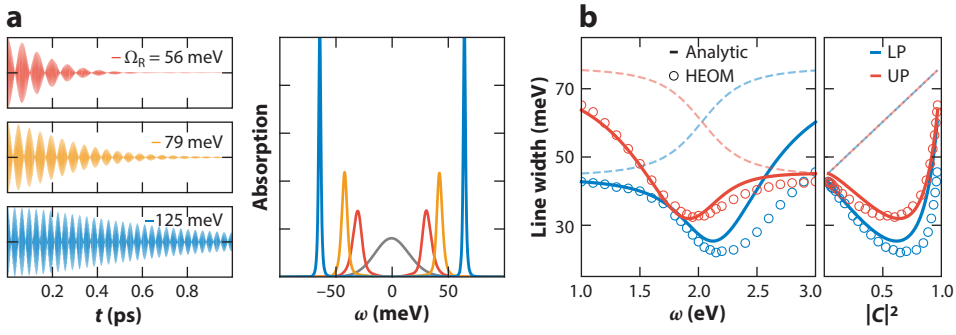

Figure 3

Polariton spectral functions and line width. (*a*) $\mathcal{A}(t)$ (*left*) and $\mathcal{A}(\omega)$ (*right*) with increasing $\hbar\Omega_R$ values: 56 meV (*red*), 79 meV (*orange*), and 125 meV (*blue*). The bare molecular absorption (*black*) is also shown on the right. (*b*) Cavity frequency dependence of the upper polariton (UP; *red*) and lower polariton (LP; *blue*) line widths. The dashed lines denote the result of Equation 15, and the solid lines denote the result of Equation 16. Open circles represent the hierarchical equations of motion (HEOM) results. Panel *a* generated using the theoretical approaches presented in Reference 87. Panel *b* adapted with permission from Reference 66.

which is even narrower than in Equation 15 and manifests as nonlinear behavior of $\Gamma_\pm$ as a function of $|C|^2$, as observed in experiments (80, 81) and in HEOM simulations of the HTC model (**Figure 3*b***).

For generally detuned cases ($\Delta_\omega \neq 0$), to the best of our knowledge, there is no simple closed-form theoretical expression for $\Gamma_\pm$. A widely used expression (79–81, 102) suggests that $\Gamma_- \propto (|C|^4/|X|^2)\Gamma$, emphasizing the nonlinear dependence of the LP line width on $|C|^2$. This finding was recently confirmed by Rury and colleagues (80, 81) through an Andersen superexchange argument. By fitting the HEOM simulation with up to $N = 8$ (**Figure 3*b***), we find (66)

$$\Gamma_- = |X|^2\kappa + \frac{1}{N}\frac{|C|^4}{|X|^2 + |C|^4/N}\Gamma, \quad \Gamma_+ = |C|^2\kappa + \frac{1}{N}\frac{|X|^4}{|C|^2 + |X|^4/N}\Gamma + \hbar k_{+\to \mathrm{D}}, \qquad 16.$$

where the matter component line width is narrowed by a factor of $1/N$ because of the polaron decoupling effect for Lorentzian lineshape (66). In Equation 16, the $\hbar k_{+\to \mathrm{D}}$ term (see Equation 13*a*) accounts for the $|+\rangle \to \{|\mathrm{D}_k\rangle\}$ relaxation (non-Condon effects) (79, 103–105), causing additional broadening of the UP line width (80, 81). As shown in **Figure 3*b***, Equation 16 accurately captures the nonlinear dependence of $\Gamma_\pm$ on $|C|^2$ compared with the HEOM results, whereas Equation 15 does not.

4. POLARITON-MEDIATED ELECTRON TRANSFER

Recent experiments by Ebbesen and colleagues (3) showed that the rate of photoisomerization reaction from merocyanine to spiropyran can be suppressed by resonantly coupling the merocyanine to a cavity, although the interpretation of such cavity modification is still under debate (106, 107). For the same reaction, Delor and colleagues (36) showed that the cavity frequency can be tuned to funnel photoexcitations into specific reactant isomers. Kalow, Stern, and colleagues (35) demonstrated that collective strong coupling to a resonant cavity can accelerate the photoisomerization of fulgide, demonstrating that the enhancement is sensitive to the collective quantity Ω_R. For a detailed review of the progress of polariton photochemistry, see Reference 5.

Despite these experimental discoveries of cavity-modified photochemistry, conceptual questions remain with regard to how local modifications of photochemistry emerge under collective strong coupling and the role of DS. To partially address these conceptual questions, we focus on simple models of a PMET reaction, which is one of the simplest photochemical reactions (17, 108–111).

4.1. Model Systems for Polariton-Mediated Electron Transfer

The model describes a total of N donor–acceptor state pairs $\{|\mathrm{D}_n\rangle, |\mathrm{A}_n\rangle\}$, both of which are molecular excited states. The donor and acceptor states are locally coupled: $\langle \mathrm{D}_n|\hat{H}_\mathrm{S}|\mathrm{A}_m\rangle = V_\mathrm{DA} \cdot \delta_{nm}$. The donor state $|\mathrm{D}_n\rangle$ (not to be confused with the DS $|\mathrm{D}_k\rangle$ in Equation 10) is considered a bright exciton state (denoted as $|\mathrm{E}_n, 0\rangle$ in Equation 5, above). The donor states are photoexcitation states that are collectively coupled to the cavity excitation:

$$\hat{H}_\mathrm{S} = \sum_{n=1}^{N}\left[\hbar\omega_0\hat{\sigma}_n^+\hat{\sigma}_n^- + V_\mathrm{DA}\left(|\mathrm{D}_n\rangle\langle \mathrm{A}_n| + \mathrm{h.c}\right)\right] + \hat{H}_\mathrm{A} + \hbar\omega_\mathrm{c}\left(\hat{a}^\dagger\hat{a} + \frac{1}{2}\right) + \hbar g_\mathrm{c}\sum_{n=1}^{N}\left(\hat{a}^\dagger\hat{\sigma}_n^- + \hat{a}\hat{\sigma}_n^+\right), \qquad 17.$$

where $\hat{\sigma}_n^+ = |\mathrm{D}_n\rangle\langle \mathrm{G}|$ and $\hat{\sigma}_n^- = |\mathrm{G}\rangle\langle \mathrm{D}_n|$, with $|\mathrm{D}_n\rangle$ as the nth molecule's electron donor state, and the acceptor Hamiltonian is $\hat{H}_\mathrm{A} = \sum_n \hbar\omega_\mathrm{A}|\mathrm{A}_n\rangle\langle \mathrm{A}_n|$, with $|\mathrm{A}_n\rangle$ as the nth molecule's electron acceptor state. Furthermore, there is one collective solvent DOF (Marcus coordinate)

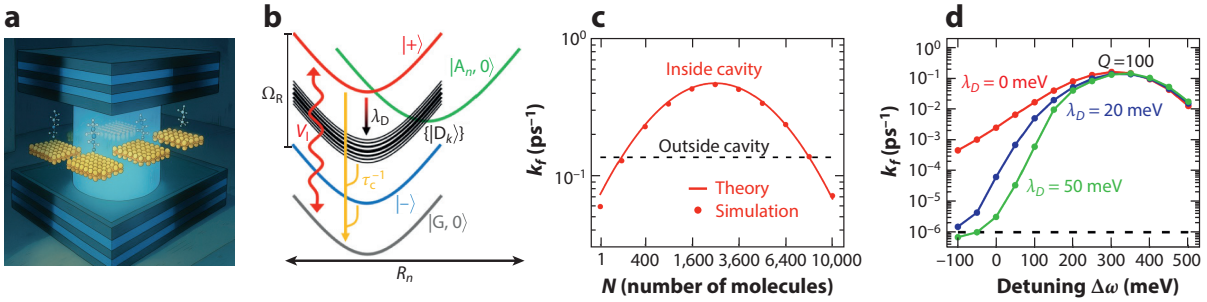

Figure 4

Model schematics and results for polariton-mediated electron transfer. (*a*) Illustration of several donor–acceptor pairs inside a cavity. (*b*) Schematic potential energy surfaces along molecule *n*'s reaction coordinate R_n with population transfer pathways resulting from laser pumping (V_1), cavity loss (τ_c^{-1}), and transfer from the upper polariton to dark states arising from energy disorder induced by λ_D. (*c*) Forward rate constants k_f as a function of N initiated from the $|+\rangle$ state (*red*) or the donor state outside the cavity (*black*). (*d*) Rate constants as a function of detuning Δ_ω for different donor reorganization energies λ_D initiated from the $|+\rangle$ state. Figure adapted with permission from Reference 108 (CC BY 3.0).

per molecular pair, R_n, which couples to both $|D_n\rangle$ and $|A_n\rangle$ states through $\hat{H}_B + \hat{H}_{SB} = \hat{T}_R + \sum_n (1/2) m_s \omega_s^2 (\hat{R}_n - R_D^0)^2 |D_n\rangle\langle D_n| + (1/2) m_s \omega_s^2 (\hat{R}_n - R_A^0)^2 |A_n\rangle\langle A_n| + (1/2) m_s \omega_s^2 \hat{R}_n^2 |G\rangle\langle G|$, where m_s is the effective solvent mass; ω_s is the effective frequency of the collective solvent DOFs; and R_D^0 and R_A^0 are the equilibrium positions of the donor and acceptor states, respectively. Each solvent DOF R_n is then coupled to a Markovian dissipative environment (for a schematic illustration of the model, see **Figure 4*a*,*b***).

4.2. Collective Polariton-Mediated Electron Transfer Mechanism

In the PMET model discussed in Section 4.1, the UP state is $|+\rangle = \sin\Theta \sum_{n=1}^{N} (1/\sqrt{N}) |D_n, 0\rangle + \cos\Theta |G, 1\rangle$ (see Equation 6). The coupling between states $|+\rangle$ and $|A_n\rangle$ is $V_{+A_n} = \langle + | \hat{H}_S | A_n, 0\rangle = (1/\sqrt{N}) \sin\Theta \cdot V_{DA}$. For an FGR rate estimation, $k_{+\to A_n} \propto |V_{+A_n}|^2 \propto 1/N$, which is often referred to as the $1/N$ dilution factor because the influence of the collective polariton state on a given molecule n is diluted by the $1/N$ factor (112). However, the collective PMET rate between the $|+\rangle$ state and all possible acceptor states is $k_{+\to A} = \sum_{n=1}^{N} k_{+\to A_n}$. Importantly, the prefactor in $k_{+\to A}$ is independent of N because of the cancellation of the $1/N$ factor in $|V_{+A_n}|^2$ with the sum over N acceptor states (1, 109). Using classical Marcus theory (FGR level of theory), one can explicitly evaluate $k_{+\to A}$ in Equation 18 as follows.

The collective PMET rate for the process $|+\rangle \to \{|A_n\rangle\}$ is expressed as

$$k_{+\to A} = \frac{1}{\hbar} \sin^2\Theta \cdot V_{DA}^2 \sqrt{\frac{\pi}{k_B T \cdot \lambda_A}} \exp\left[-\frac{(\Delta G - \hbar(\Delta_\omega + \Omega_R)/2 + \lambda_A)^2}{4 k_B T \cdot \lambda_A} \right], \quad 18.$$

where Ω_R is the Rabi splitting (Equation 9), $\Delta_\omega = \omega_c - \omega_0$ is the light–matter detuning (between the cavity and the donor exciton state), and λ_A is the acceptor reorganization energy. The collective quantity Ω_R explicitly appears in the rate constant through the modification of the effective driving force for the $|+\rangle \to \{|A_n\rangle\}$ process.

As shown in Equation 18, the only N dependence in $k_{+\to A}$ comes from the collective Rabi splitting $\Omega_R \propto 2\sqrt{N} g_c$, which changes the ET driving force. **Figure 4*c*** depicts this collective N dependence. The log of the rate constant $k_{+\to A}$ has a parabolic dependence on $\sqrt{N}$, with strong agreement between theory and simulation. This rate theory suggests a possible mechanism that depends on the collective coupling Ω_R, even though the light–matter coupling strength per molecule g_c is small. Unlike the acceptor reorganization energy λ_A, the donor reorganization energy

Acceptor reorganization energy:
$\lambda_A = (1/2) m_s (\omega_s R_A^0)^2$

ET driving force:
$\Delta G = \hbar\omega_A - \hbar\omega_0$

Donor reorganization energy:
$\lambda_D = (1/2) m_s (\omega_s R_D^0)^2$

λ_D does not explicitly appear in $k_{+\to A}$ because of the polaron decoupling effect (Equation 12). Under the large-N limit, the $|+\rangle$ state experiences an effective reorganization energy of $\lambda_D/4N \to 0$ (for arbitrary N, the expression for λ can be found in equation 20 of Reference 108). Nevertheless, λ_D governs the rate of transition from $|+\rangle$ to the DS manifold [see Equation 13*a*, where the coupling strength $c_\alpha^2 \propto \lambda_D$ in $J(\omega)$].

4.3. Challenges of Cavity Loss

Without external laser pumping of the system, cavity loss (see Section 2.1.3) can inhibit PMET by eliminating the photoexcitation inside the cavity before the excitation can transfer to the acceptor states. To address this challenge, one can tune an external continuous-wave (CW) laser to the $|G, 0\rangle \to |+\rangle$ transition, such that the $|+\rangle$ state population is constantly populated.

This interaction can be described by (18) $\hat{H}_l(t) = V_l\left(\hat{a}e^{i\omega_l t} + \hat{a}^\dagger e^{-i\omega_l t}\right)$, with pumping strength V_l and laser frequency $\omega_l = \omega_+$, as done in Reference 108. This CW laser pumping can replenish lost cavity photons back to the UP state and reenable PMET to the acceptor states. The simulations of the $k_{+\to A}$ rate constants shown in **Figure 4*d*** use CW laser pumping to replenish the $|+\rangle$ state population inside a lossy $\mathcal{Q} = 100$ cavity.

4.4. Challenges of Decay to Dark States

Disorder in the energies or dipole orientations of molecules coupled to the cavity causes population transfer between bright polariton states and DS. The PMET model considered here does not contain explicit static energy disorder but rather experiences thermal-induced energy disorder with an effective donor line width of $\sigma = \sqrt{2\lambda_D k_B T}$ arising from the donor reorganization energy λ_D. This disorder causes population transfer primarily from the $|+\rangle$ and $|-\rangle$ states to the DS. This population transfer can inhibit PMET enhancement by trapping the population in the DS, which undergo significantly slower ET than the $|+\rangle$ state.

To address this challenge, one can significantly reduce the transfer rate from the $|+\rangle$ state to the DS by increasing both the Rabi splitting Ω_R and the cavity detuning Δ_ω (108). These increases widen the energy gap between the $|+\rangle$ state and the DS, which in turn can significantly reduce the transfer rate to the DS as a result of the phonon bottleneck effect (92), thereby allowing for faster PMET from the $|+\rangle$ state. The effect of increasing Δ_ω on the simulated $k_{+\to A}$ rate constants is shown in **Figure 4*d***, where larger, positive detunings cause significantly enhanced transfer to the acceptor states compared with resonance ($\Delta_\omega = 0$) for molecules with thermal-induced disorder ($\lambda_D > 0$). Additionally, the rate constants for large detunings $\Delta_\omega > 300$ meV become independent of λ_D as a result of a large phonon bottleneck effect that diminishes the effect of the DS.

5. VIBRATIONAL STRONG COUPLING–ENABLED POLARITON CHEMISTRY

VSC emerges from the interaction between molecular vibrations and quantized radiation modes in an optical cavity. Recent experiments (37–40, 46, 113–116) have shown that VSC can modify ground-state chemical reactivity by either resonantly suppressing or enhancing the reaction rates, thus offering new strategies in synthetic chemistry. Key features of VSC-modified reactivity include (*a*) a resonance effect when the cavity frequency matches that of a molecular vibration (37, 40), (*b*) a maximum effect at normal incidence (37), (*c*) enhancement in the magnitude of the modification with increasing molecular density (collective effect) (37, 38, 46), and (*d*) changes in reactivity in the absence of optical pumping (thermal activation) (37, 39).

A clear mechanistic understanding remains elusive, despite exciting theoretical progress (47, 48, 117–123). In particular, all of the existing classic ground-state reaction rate theories [e.g.,

transition-state theory (TST), Grote–Hynes theory (120, 124), quantum TST (125), Pollak–Grabert–Hänggi theory (121, 123)] and molecular dynamics simulations [e.g., Langevin dynamics (126), ring polymer molecular dynamics (127)] fail when used to explain the VSC effects. The conceptual hypothesis is that the cavity mode can be viewed and treated as regular nuclear vibrations (120). Unfortunately, none of these theories have successfully predicted the correct resonance condition or the sharp resonance peak of the rate constant distribution (120, 121, 125, 126). Note that the quantum transition path theory recently developed by Limmer and colleagues (128) can produce a sharp resonance suppression peak, but it does not capture the correct resonance peak position because of the anharmonicity of the reaction coordinate. More recent studies (129–133) have emphasized the importance of a full quantum description of the vibrational DOF and/or the photonic DOF and have shown that strong coupling of a reaction coordinate with a cavity mode boosts the rate constant. An analytic theory to describe this enhancement has been formulated (130, 134) and extended to many cavity mode coupling cases to demonstrate the resonance conditions at normal incidence (134–136).

At present, a clear understanding of the first, second, and fourth key experimental features mentioned above has been achieved; however, the third experimental feature—the collective effect—remains an important open question. The reason is that, under collective light–matter coupling, the effects observed under the single-molecule strong coupling condition usually become minimal because of the large-N dilution (47, 118, 123) and isotropic disorder effects (124). To address this issue, we developed a quantum mechanical rate theory for a model ground-state reaction coupled to a cavity mode (124) that captures the abovementioned basic features of VSC experiments (136), especially the resonance and the collective behavior of the rate constant modifications.

5.1. Model System for Vibrational Strong Coupling

We consider a theoretical model where a cavity mode couples to a set of solvent vibrations $\{\mathcal{R}_n\}$ (spectator modes, or rate-promoting vibrations) that, in turn, couple to a reaction coordinate R_0 (**Figure 5*a***). Instead of the approximated TC-type light–matter interaction Hamiltonian, we use the Pauli–Fierz Hamiltonian (1) to describe the molecular vibrations collectively coupled to a mode in an optical cavity (124): $\hat{H} = \hat{H}_S(\hat{R}_0, \{\hat{\mathcal{R}}_n\}) + \hat{H}_v + \hat{H}_{loss}$ (where $\hat{H}_S$ is the system Hamiltonian that contains the vibrational and photonic DOFs, as well as their couplings; $\hat{H}_v$ is the dissipative environmental DOF that further couples to R_0 and $\{\mathcal{R}_n\}$; and $\hat{H}_{loss}$ is the cavity loss Hamiltonian, as described in Section 2.1.3). The system Hamiltonian is expressed as

$$\hat{H}_S = \hat{H}_0 + \sum_{n=1}^{N}\left[\frac{1}{2}\hat{\mathcal{P}}_n^2 + \frac{1}{2}\omega_0^2\left(\hat{\mathcal{R}}_n - \frac{\mathcal{C}_n}{\omega_0^2}\hat{R}_0\right)^2\right] + \left[\frac{\hat{p}_c^2}{2} + \frac{\omega_c^2}{2}\left(\hat{q}_c + \sqrt{\frac{2}{\omega_c}}\eta_c\sum_{n=1}^{N}\hat{\mathcal{R}}_n\right)^2\right], \quad 19.$$

where $\hat{H}_0 = \hat{T}_0 + \hat{V}(\hat{R}_0)$, with $\hat{R}_0$ as the reaction coordinate, and $\hat{V}(\hat{R}_0)$ is the ground-state PES (symmetric double-well potential along $\hat{R}_0$). The nonreactive spectator modes $\{\mathcal{R}_n\}$ have identical frequencies ω_0 and are linearly coupled to $\hat{R}_0$ through $\mathcal{C}_n$. This model captures the key features of recent VSC experiments (37, 40) and has been employed in theoretical studies of VSC-modified reactivities (124, 129). It also reflects the characteristics observed in theoretical simulations of polaritonic vibrational energy relaxation (137), which demonstrate collective and resonance behavior. For example, in Reference 37, C–Si is the R_0 reaction coordinate, and Si–$(Me)_3$ is the nonreactive $\mathcal{R}_n$ mode that strongly couples to R_0 (for $N = 1$). In Reference 40, the spectator mode $\mathcal{R}_n$ could be the N–C–O vibrational mode in the reactant (for $N = 1$). The solvent vibrations could also be viewed as the spectator mode $\{\mathcal{R}_n\}$ (for $N \gg 1$), which was explored in recent VSC theoretical investigations (124, 129).

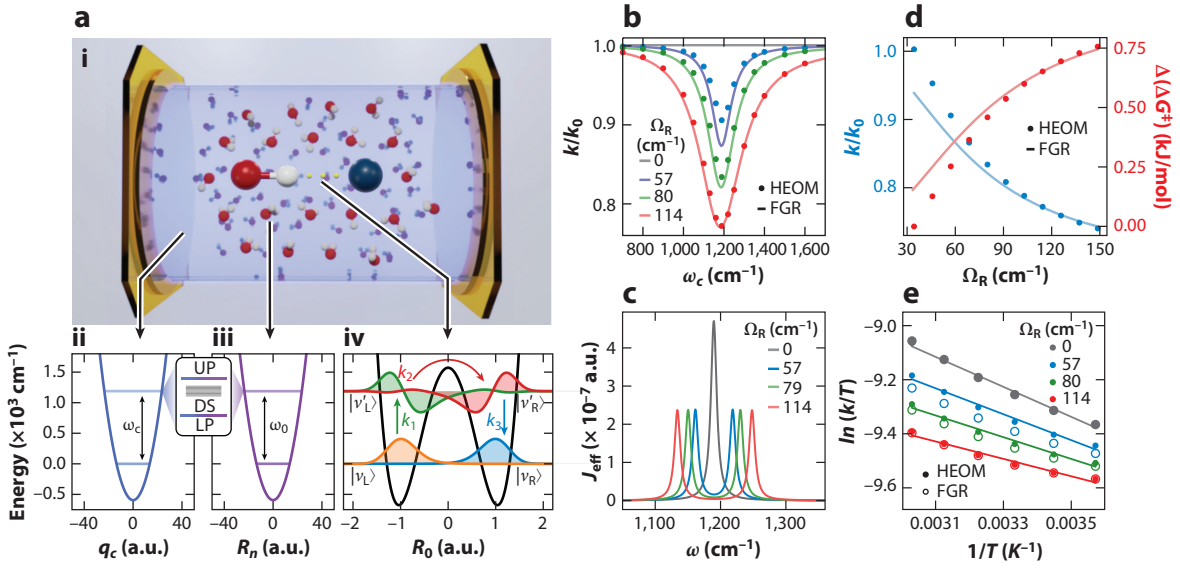

Figure 5

Model schematics and results for vibrational strong coupling–modified ground-state chemistry. (*a*) Schematic illustration of a set of solvent vibrations coupled to the cavity radiation field as well as a reaction coordinate. (*b*) Normalized rate constant profile (with respect to the outside cavity case k_0) as a function of cavity frequency ω_c at different $\hbar\Omega_R$. Solid lines represent the Fermi's golden rule (FGR) expression (Equation 22), and dots represent the hierarchical equations of motion (HEOM) results. (*c*) Effective spectral density $J_{\text{eff}}(\omega)$ (Equation 22) for different $\hbar\Omega_R$ values. The two peaks correspond to the polariton modes. (*d*) Ratio of the rate constant inside the cavity to the rate constant outside the cavity, and effective free-energy barrier change $\Delta(\Delta G^{\ddagger})$ at resonance as a function of $\hbar\Omega_R$. The blue curve indicates that suppression effects on k/k_0 increase with a Ω_R^2 scaling. Red indicates the change of $\Delta(\Delta G^{\ddagger})$ through $\Delta(\Delta G^{\ddagger}) = \Delta G^{\ddagger} - \Delta G_0^{\ddagger} = -k_B T \ln(k/k_0)$. (*e*) Eyring plot at various $\hbar\Omega_R$ (at resonance). Black represents the temperature dependence of the rate constant outside the cavity, and colors represent the temperature dependence inside the cavity. Filled circles represent HEOM results, and open circles represent the FGR theory. Note that we have neglected $\hbar$ in all panels that are associated with Ω_R. Abbreviations: DS, dark states; LP, lower polariton; UP, upper polariton. Figure adapted with permission from Reference 136 (CC BY 4.0).

In the last term of Equation 19, $\hat{q}_c = \sqrt{\hbar/(2\omega_c)}(\hat{a}^\dagger + \hat{a})$ and $\hat{p}_c = i\sqrt{\hbar\omega_c/2}(\hat{a}^\dagger - \hat{a})$ are the cavity field operators, where ω_c is the cavity frequency and $\eta_c = \sqrt{1/(2\hbar\omega_c\epsilon_0\mathcal{V})}$ is the light–matter coupling strength. Note that in Equation 19 we have assumed that the vibrational transition dipole operators are linear (118, 120, 129), such that $\hat{\boldsymbol{\mu}}(\mathcal{R}_n)\cdot\hat{\mathbf{e}} \approx \hat{\mathcal{R}}_n \cdot \cos\varphi_n \approx \hat{\mathcal{R}}_n$ (no orientation disorder), where $\hat{\mathbf{e}}$ is the field polarization direction. Under the resonance condition, the overall Rabi splitting (1, 45, 47) is expressed as $\Omega_R = 2\sqrt{N}\eta_c\omega_c\langle 0|\hat{\mu}(\mathcal{R}_n)|1\rangle \approx 2\sqrt{N}\eta_c\omega_c\langle 0|\hat{\mathcal{R}}_n|1\rangle$ (where $|0\rangle$ and $|1\rangle$ are the ground and first excited states of $\mathcal{R}_n$). The cavity mode couples collectively to all solvent modes $\{\mathcal{R}_n\}$ through η_c, resulting in delocalized interactions that can be observed from the Rabi splitting in spectroscopy (138).

5.2. Reaction Mechanism and Hypothesis

Under a thermal initial condition, the reaction coordinate R_0 undergoes a barrier-crossing process (139, 140), where the transition state is reached and finally relaxes to the product configuration. Quantum mechanically, this process is described as

$$|\nu_L\rangle \xrightarrow{k_1} |\nu_L'\rangle \xrightarrow{k_2} |\nu_R'\rangle \xrightarrow{k_3} |\nu_R\rangle, \qquad 20.$$

Vibrational transition amplitude: $\Delta = \langle \nu_L | \hat{R}_0 | \nu'_L \rangle$

where the system is first thermally excited from the vibrational ground state ($|\nu_L\rangle$) to the excited state ($|\nu'_L\rangle$) of the left side of the well (reactant). This excited state then tunnels to a vibrational excited state ($|\nu'_R\rangle$) on the right side of the well (product), which relaxes to its ground state ($|\nu_R\rangle$) (subpanel *iv* of **Figure 5*a***). The vibrational frequency $\omega_0 \equiv (E_{\nu'_L} - E_{\nu_L})/\hbar$ of the reactant corresponds to the transition $|\nu_L\rangle \rightarrow |\nu'_L\rangle$ and is chosen to match the frequency of $\{\mathcal{R}_n\}$. Exact quantum dynamics simulations suggest that, under the energy diffusion–limited regime of the reaction [before Kramers turnover (139, 140)], the initial vibrational excitation ($|\nu_L\rangle \rightarrow |\nu'_L\rangle$) is rate limiting, with $k_1 \ll k_2, k_3$. This rate limiting in vibrational excitation leads to a steady-state population of the intermediate states $|\nu'_L\rangle$ and $|\nu'_R\rangle$, and the overall reaction rate is given approximately by $k \approx k_1$. However, when the reaction barrier is low, k_1 is no longer rate limiting and cavity coupling no longer significantly affects the overall rate. This result may explain the absence of VSC effects in low-barrier reactions (141, 142).

The $|\nu_L\rangle \rightarrow |\nu'_L\rangle$ transition is driven mainly by the energy exchange between the reaction coordinate R_0 and the spectator modes $\{\mathcal{R}_n\}$. When these modes are resonantly coupled to the cavity, the light–matter hybrid system has a set of polaritonic modes with frequencies $\omega_\pm = \omega_0 \pm \Omega_R/2$, effectively shifting energy away from ω_0 and thus suppressing the influence of $\{\mathcal{R}_n\}$ on the $|\nu_L\rangle \rightarrow |\nu'_L\rangle$ transition. This suppression can also be understood as a fast energy exchange among the strongly coupled $\{\mathcal{R}_n\}$ and $\hat{q}_c$ at the Rabi frequency Ω_R. This energy redistribution effectively decouples $\{\mathcal{R}_n\}$ from the $|\nu_L\rangle \rightarrow |\nu'_L\rangle$ transition, reducing the value of k_1. Because this step remains rate limiting for the reaction process, the influence of the cavity on k_1 manifests in the entire apparent rate constant of the reaction, as $k \approx k_1$.

According to this mechanism, the impact of VSC on the rate is attributable solely to the cavity interacting with the spectator modes. This hypothesis has been confirmed by quantum dynamics simulations (see figure S2 of Reference 136), where the steady-state population of the $|\nu'_L\rangle$ state is reduced when coupled to the cavity. To quantify the effect of the cavity on the chemical reactivity, we express the ratio of the rate constant inside the cavity to the rate constant outside the cavity as

$$k/k_0 = k_D/k_0 + \alpha \cdot k_{VSC}/k_0, \qquad 21.$$

where k_0 is the rate constant outside the cavity, k_D is the rate constant for the double-well potential without coupling to any spectator modes $\{\mathcal{R}_n\}$ or the cavity mode q_c, and k_{VSC} is the contribution of the spectator modes to the overall rate, with α as a constant scaling parameter. Outside the cavity, the ratio k_{VSC}/k_0 peaks when $\{\mathcal{R}_n\}$ modes resonate with the transition $|\nu_L\rangle \rightarrow |\nu'_L\rangle$, enhancing vibration along R_0. Inside the cavity, this ratio lessens with light–matter coupling and eventually reaches zero because the modes no longer affect the rate, with $k \sim k_D$. This effect indicates a polaron decoupling effect (51, 52, 66, 119) wherein cavity and spectator mode resonance inhibits energy flow to R_0, enabling an analytic rate constant theory based on FGR, consistent with VSC findings.

We use FGR to evaluate the $|\nu_L\rangle \rightarrow |\nu'_L\rangle$ transition rate constant, resulting in

$$k_{VSC} = 2|\Delta|^2 \int_0^\infty d\omega \frac{\Lambda\omega_0^2 \cdot \omega\Gamma_{\mathcal{R}}(\omega)}{\left[\omega_0^2 - \omega^2 + \Pi(\omega)\right]^2 + [\omega\Gamma_{\mathcal{R}}(\omega)]^2} \mathcal{A}_0(\omega - \omega_0) e^{-\beta\hbar\omega_0}. \qquad 22.$$

Here, ω_0 is the vibrational frequency for $\{\mathcal{R}_n\}$, with $n \in \{1, \ldots, N\}$, as well as for reaction coordinate R_0; Δ is the vibrational transition amplitude for $|\nu_L\rangle \rightarrow |\nu'_L\rangle$ associated with R_0; and $\mathcal{A}_0(\omega - \omega_0)$ accounts for the broadening of this transition due to the local environmental fluctuations. In addition, $\Gamma_{\mathcal{R}}$ characterizes the excitation decay rate in the $\{\mathcal{R}_n\}$ and cavity modes, and $\Pi(\omega)$ characterizes the cavity effect over $\{\mathcal{R}_n\}$. These are expressed as

$$\Gamma_{\mathcal{R}}(\omega) = \frac{2N\eta_c^2 \cdot \omega_c^3 \tau_c^{-1}}{\left(\omega_c^2 - \omega^2\right)^2 + \omega^2\tau_c^{-2}} + \frac{2\lambda_{\mathcal{R}}}{\gamma_{\mathcal{R}}}, \quad \Pi(\omega) = 2N\eta_c^2\omega_c\omega^2 \cdot \frac{(\omega^2 - \omega_c^2 + \tau_c^{-2})}{\left(\omega_c^2 - \omega^2\right)^2 + \omega^2\tau_c^{-2}},$$

where $\lambda_{\mathcal{R}}$ and $\gamma_{\mathcal{R}}$ are phonon bath parameters for $\{\mathcal{R}_n\}$ modes with a spectral density $J(\omega) = (2\lambda_{\mathcal{R}}\gamma_{\mathcal{R}}\omega)/(\omega^2 + \gamma_{\mathcal{R}}^2)$. Interestingly, k_{VSC} contains collective quantities, including the collective Rabi splitting $\Omega_{\mathrm{R}}^2 \propto N g_{\mathrm{c}}^2$, as well as the collective solvent reorganization energy $\Lambda = \sum_{n=1}^{N} \mathcal{C}_n^2/2\omega_0^2$ that accounts for the interactions between $\{\mathcal{R}_n\}$ and R_0.

Solvent reorganization energy: $\Lambda = \sum_{n=1}^{N} \mathcal{C}_n^2/2\omega_0^2$

5.3. Behavior of the Rate Theory and Connections with Experiments

We briefly discuss the key features of the rate constant theory in Equation 22 and its connection with experiments.

5.3.1. Resonance suppression. The analytic theory k_{VSC} predicts a sharp resonance suppression of the rate constant. **Figure 5*b*** presents the cavity frequency dependence of k/k_0 with the maximum suppression achieved at $\omega_{\mathrm{c}} = \omega_0$. The FGR expression (Equation 22) accurately captures the cavity frequency dependence of the rate constants for a wide range of Ω_{R}, in agreement with HEOM results. This suppression can be interpreted from the effective spectral density $J_{\mathrm{eff}}(\omega)$ (**Figure 5*c***; Equation 22) as it accounts for the effective coupling from $\{\mathcal{R}_n\}$ on R_0. Coupling the cavity splits $J_{\mathrm{eff}}(\omega)$ into two peaks. The separation between these peaks and the $|\nu_{\mathrm{L}}\rangle \rightarrow |\nu_{\mathrm{L}}'\rangle$ transition is proportional to Ω_{R}, with frequencies that are nearly identical to the vibrational polariton frequencies. Note that the dark modes in this model do not couple to R_0 as a result of symmetry. As such, k_{VSC} in Equation 22 quantitatively matches the HEOM results and is capable of describing the sharp resonance behavior observed in experiments (37, 40).

5.3.2. Scaling with the collective Rabi splitting. Under the resonance condition $\omega_{\mathrm{c}} = \omega_0$, Equation 22 predicts that $k_{\mathrm{VSC}} \propto 1/\Omega_{\mathrm{R}}^2 \propto 1/(N\eta_{\mathrm{c}}^2)$. This prediction implies that suppression effects on k/k_0 increase with a Ω_{R}^2 scaling (**Figure 5*d***). This trend closely resembles experimental observations (see, e.g., figure 3D of Reference 46).

These rate constant changes can be interpreted as the change of the effective free-energy barrier $\Delta(\Delta G^{\ddagger})$ through (38, 46, 130) $\Delta(\Delta G^{\ddagger}) = \Delta G^{\ddagger} - \Delta G_0^{\ddagger} = -k_{\mathrm{B}}T \ln(k/k_0)$ (**Figure 5*d***). However, this is not an actual change in the free-energy barrier but rather an effective measure of a purely kinetic effect. The figure shows a nonlinear relation of $\Delta(\Delta G^{\ddagger})$ with Ω_{R} that agrees with what has been observed experimentally (e.g., figure 3c of Reference 46). Future experimental investigations should focus on measuring more data points to determine the fundamental scaling relations.

5.3.3. Temperature dependence. The temperature dependence of the rate constant is often understood through the Eyring equation (46) based on TST: $\ln(k/T) \propto -(\Delta H^{\ddagger})/(k_{\mathrm{B}})\cdot 1/T + (\Delta S^{\ddagger})/k_{\mathrm{B}}$. **Figure 5*e*** presents the temperature dependence of the rate constant outside and inside the cavity. Here, both HEOM simulations and the FGR theory predict the same trend for the changes in $\Delta H^{\ddagger}$ and $\Delta S^{\ddagger}$ as a function of Ω_{R}, which has been experimentally observed (46, 143). We emphasize that, based on our current theory, the VSC reaction mechanism is not related to the direct modification of $\Delta H^{\ddagger}$ nor $\Delta S^{\ddagger}$ [as proposed by earlier theories (120)] but rather pertains to how the cavity can mediate vibrational excitations, in particular, by modifying the rate constant k_1 associated with the $|\nu_{\mathrm{L}}\rangle \rightarrow |\nu_{\mathrm{L}}'\rangle$ transition (see Equation 20). Thus, the changes in the rate constant are purely kinetic.

5.3.4. Resonance effect at normal incidence. According to the photon dispersion in a Fabry–Pérot cavity (Equation 2), there are still a finite number of modes (with $k_{\parallel} \neq 0$), such that $\omega_{\mathbf{k}} = \omega_0$ (oblique incidence). However, although polaritons form under this condition, VSC effects are observed only at $k_{\parallel} = 0$ (normal incidence) (37, 47, 143). This normal incidence condition arises from the photonic mode density of states inside the cavity, which peaks at $k_{\parallel} \approx 0$ (134–136), thereby enhancing the VSC contribution at the normal incidence. The generalization

of the k_{VSC} expression to include integration over the photonic mode density of states indicates that, at $k_{\parallel} = 0$, the photonic mode has no in-plane momentum and is spatially confined. This confinement increases the photon's lifetime, leading to the greatest magnitude of rate suppression. In contrast, at $k_{\parallel} \neq 0$, the photonic mode has a finite in-plane momentum, reducing its effective lifetime in a given mode volume (135) and thereby weakening the cavity effects on the system.

5.4. Limitations and Effect of Disorder

The model considered above does not take into account disorder in the $\{\mathcal{R}_n\} - R_0$ coupling ($\mathcal{C}_n$ in Equation 19) and the angle between the cavity field polarization and molecular dipole moments (φ_n). In Reference 136, we explicitly consider such disorder and show that the $J_{\text{eff}}(\omega)$ will gradually grow a peak at $\omega = \omega_0$, which are the vibrational DS. Increasing the magnitude of disorder [in either $\mathcal{C}_n$ or φ_n in the light–matter coupling term $\hat{\boldsymbol{\mu}}(\mathcal{R}_n) \cdot \hat{\mathbf{e}} \approx \hat{\mathcal{R}}_n \cdot \cos\varphi_n$] leads to the appearance of these DS in the effective spectral density that couple to R_0, which will influence the rate constant in the same way as outside the cavity. As a result, cavity effects can persist only under moderate disorder (see figure 5 of Reference 136), whereas they diminish under an isotropic distribution of φ_n or a broad variation in $\mathcal{C}_n$.

6. CONCLUSIONS AND PERSPECTIVE

In this review, we have highlighted the necessary theoretical components in a description of collective light–matter coupling for many molecules and optical cavity modes. The collective effects are exhibited in more ways than one for various polaritonic systems—for example, the reduced reorganization energy due to the polaron decoupling effect, the modification of the ET driving force, and the effective spectral density in VSC. Furthermore, we have addressed several open questions and controversies in the field. We began with the HTC Hamiltonian that describes collective light–matter coupling and introduced the concept of polariton states and DS. For polariton photophysics, we discussed the well-understood polariton relaxation dynamics, the decoherence process, and spectral properties—particularly the motional narrowing effect. These polariton photophysical properties are closely related to the polaron decoupling effect. For polariton photochemistry, we considered a model for the PMET reaction, where the collective quantity Ω_R explicitly appears in the rate constant expression (to modify the ET driving force). For VSC, we considered a model in which the solvent (spectator vibrations) is collectively coupled to the cavity mode, as well as a reaction coordinate, where both Ω_R and solvent reorganization energy Λ (also a collective quantity) show up in the rate constant modification. These theoretical investigations shed light on how collective light–matter coupling could influence polariton dynamics, coherence, spectroscopy, photochemical reactions, and VSC chemistry. Future investigations should focus on exploring the validity of the proposed mechanisms with experimental measurements as well as on testing the scaling relations predicted by the analytic expressions in, for example, Equations 18 and 22. Ultimately, the collective strong coupling regime represents not merely a perturbation to matter but rather a fundamentally new avenue for controlling quantum states and designing hybrid light–matter systems. As our understanding deepens, it holds the promise to redefine paradigms in chemistry, physics, and materials science alike.

DISCLOSURE STATEMENT

The authors are not aware of any affiliations, memberships, funding, or financial holdings that might be perceived as affecting the objectivity of this review.

ACKNOWLEDGMENTS

The writing of this review was supported by the Air Force Office of Scientific Research under award FA9550-23-1-0438. W.Y. appreciates the support of a Moses Passer Graduate Fellowship from the University of Rochester (U of R). S.M.V. appreciates the support of an Esther M. Conwell Graduate Fellowship and an Elon Huntington Hooker Fellowship from U of R. M.E.M. appreciates the support of a Wu Fellowship and a Messersmith Dissertation Fellowship from U of R. P.H. appreciates the support of a Cottrell Scholar Award (a program by the Research Corporation for Science Advancement). We appreciate the valuable contributions of polariton coherence simulations by Ben Chng, development of nonequilibrium rate theory by Yifan Lai, and development of the collective PMET and VSC mechanisms by Arkajit Mandal. W.Y. acknowledges valuable comments from Xuecheng Tao. We appreciate valuable discussions with Milan Delor, Andrew Musser, Tal Schwartz, Minjung Son, Aaron Rury, Steve Cundiff, Nick Vamivakas, and Todd Krauss.

LITERATURE CITED

1. Mandal A, Taylor MA, Weight BM, Koessler ER, Li X, Huo P. 2023. Theoretical advances in polariton chemistry and molecular cavity quantum electrodynamics. *Chem. Rev.* 123:9786–879
2. Schwartz T, Hutchison JA, Genet C, Ebbesen TW. 2011. Reversible switching of ultrastrong light–molecule coupling. *Phys. Rev. Lett.* 106:196405
3. Hutchison JA, Schwartz T, Genet C, Devaux E, Ebbesen TW. 2012. Modifying chemical landscapes by coupling to vacuum fields. *Angew. Chem. Int. Ed.* 51:1592–96
4. Ebbesen TW. 2016. Hybrid light–matter states in a molecular and material science perspective. *Acc. Chem. Res.* 49:2403–12
5. Bhuyan R, Mony J, Kotov O, Castellanos GW, Rivas JG, et al. 2023. The rise and current status of polaritonic photochemistry and photophysics. *Chem. Rev.* 123:10877–919
6. Xiang B, Ribeiro RF, Du M, Chen L, Yang Z, et al. 2020. Intermolecular vibrational energy transfer enabled by microcavity strong light–matter coupling. *Science* 368:665–67
7. Chen TT, Du M, Yang Z, Yuen-Zhou J, Xiong W. 2022. Cavity-enabled enhancement of ultrafast intramolecular vibrational redistribution over pseudorotation. *Science* 378:790–94
8. Xiong W. 2023. Molecular vibrational polariton dynamics: What can polaritons do? *Acc. Chem. Res.* 56:776–86
9. Xiang B, Xiong W. 2024. Molecular polaritons for chemistry, photonics and quantum technologies. *Chem. Rev.* 124:2512–52
10. Hirschmann O, Bhakta HH, Xiong W. 2024. The role of IR inactive mode in $W(CO)_6$ polariton relaxation process. *Nanophotonics* 13:2029–34
11. Semenov A, Nitzan A. 2019. Electron transfer in confined electromagnetic fields. *J. Chem. Phys.* 150:174122
12. Chowdhury SN, Mandal A, Huo P. 2021. Ring polymer quantization of the photon field in polariton chemistry. *J. Chem. Phys.* 154:044109
13. Saller MAC, Lai Y, Geva E. 2022. An accurate linearized semiclassical approach for calculating cavity-modified charge transfer rate constants. *J. Phys. Chem. Lett.* 13:2330–37
14. Saller MAC, Lai Y, Geva E. 2023. Cavity-modified Fermi's golden rule rate constants: beyond the single mode approximation. *J. Chem. Phys.* 159:151105
15. Saller MAC, Lai Y, Geva E. 2023. Cavity-modified Fermi's golden rule rate constants from cavity-free inputs. *J. Phys. Chem. C* 127:3154–64
16. Sharma SK, Chen HT. 2024. Unraveling abnormal collective effects via the non-monotonic number dependence of electron transfer in confined electromagnetic fields. *J. Chem. Phys.* 161:104102
17. Mandal A, Krauss TD, Huo P. 2020. Polariton-mediated electron transfer via cavity quantum electrodynamics. *J. Phys. Chem. B* 124:6321–40

18. Qiu L, Mandal A, Morshed O, Meidenbauer MT, Girten W, et al. 2021. Molecular polaritons generated from strong coupling between CdSe nanoplatelets and a dielectric optical cavity. *J. Phys. Chem. Lett.* 12:5030–38
19. Peng K, Rabani E. 2023. Polaritonic bottleneck in colloidal quantum dots. *Nano Lett.* 23:10587–93
20. Morshed O, Amin M, Cogan NMB, Koessler ER, Collison R, et al. 2024. Room-temperature strong coupling between CdSe nanoplatelets and a metal–DBR Fabry–Pérot cavity. *J. Chem. Phys.* 161:014710
21. Amin M, Koessler ER, Morshed O, Awan F, Cogan NMB, et al. 2024. Cavity controlled upconversion in CdSe nanoplatelet polaritons. *ACS Nano* 18:21388–98
22. Hou S, Khatoniar M, Ding K, Qu Y, Napolov A, et al. 2020. Ultralong-range energy transport in a disordered organic semiconductor at room temperature via coherent exciton-polariton propagation. *Adv. Mater.* 32:2002127
23. Pandya R, Chen RYS, Gu Q, Sung J, Schnedermann C, et al. 2021. Microcavity-like exciton-polaritons can be the primary photoexcitation in bare organic semiconductors. *Nat. Commun.* 12:6519
24. Pandya R, Ashoka A, Georgiou K, Sung J, Jayaprakash R, et al. 2022. Tuning the coherent propagation of organic exciton-polaritons through dark state delocalization. *Adv. Sci.* 9:2105569
25. Xu D, Mandal A, Baxter JM, Cheng SW, Lee I, et al. 2023. Ultrafast imaging of polariton propagation and interactions. *Nat. Commun.* 14:3881
26. Cheng SW, Xu D, Su H, Baxter JM, Holtzman LN, et al. 2023. Optical imaging of ultrafast phonon-polariton propagation through an excitonic sensor. *Nano Lett.* 23:9936–42
27. Balasubrahmaniyam M, Simkhovich A, Golombek A, Sandik G, Ankonina G, Schwartz T. 2023. From enhanced diffusion to ultrafast ballistic motion of hybrid light–matter excitations. *Nat. Mater.* 22:338–44
28. Sandik G, Feist J, García-Vidal FJ, Schwartz T. 2025. Cavity-enhanced energy transport in molecular systems. *Nat. Mater.* 24:344–55
29. Ying W, Chng BX, Delor M, Huo P. 2025. Microscopic theory of polariton group velocity renormalization. *Nat. Commun.* 16:6950
30. Cao J. 2022. Generalized resonance energy transfer theory: applications to vibrational energy flow in optical cavities. *J. Phys. Chem. Lett.* 13:10943–51
31. Sokolovskii I, Tichauer RH, Morozov D, Feist J, Groenhof G. 2023. Multi-scale molecular dynamics simulations of enhanced energy transfer in organic molecules under strong coupling. *Nat. Commun.* 14:6613
32. Peng K, Rabani E. 2024. Polariton-assisted incoherent to coherent excitation energy transfer between colloidal nanocrystal quantum dots. *J. Chem. Phys.* 161:154107
33. Angelakis DG, ed. 2017. *Quantum Simulations with Photons and Polaritons: Merging Quantum Optics with Condensed Matter Physics*. Springer International Publishing
34. Ghosh S, Liew TC. 2020. Quantum computing with exciton-polariton condensates. *npj Quantum Inf.* 6:16
35. Zeng H, Pérez-Sánchez JB, Eckdahl CT, Liu P, Chang WJ, et al. 2023. Control of photoswitching kinetics with strong light–matter coupling in a cavity. *J. Am. Chem. Soc.* 145:19655–61
36. Lee I, Melton SR, Xu D, Delor M. 2024. Controlling molecular photoisomerization in photonic cavities through polariton funneling. *J. Am. Chem. Soc.* 146:9544–53
37. Thomas A, George J, Shalabney A, Dryzhakov M, Varma SJ, et al. 2016. Ground-state chemical reactivity under vibrational coupling to the vacuum electromagnetic field. *Angew. Chem. Int. Ed.* 55:11462–66
38. Lather J, Bhatt P, Thomas A, Ebbesen TW, George J. 2019. Cavity catalysis by cooperative vibrational strong coupling of reactant and solvent molecules. *Angew. Chem. Int. Ed.* 58:10635–38
39. Thomas A, Lethuillier-Karl L, Nagarajan K, Vergauwe RMA, George J, et al. 2019. Tilting a ground-state reactivity landscape by vibrational strong coupling. *Science* 363:615–19
40. Ahn W, Triana JF, Recabal F, Herrera F, Simpkins BS. 2023. Modification of ground-state chemical reactivity via light–matter coherence in infrared cavities. *Science* 380:1165–68
41. Müller K, Fischer KA, Rundquist A, Dory C, Lagoudakis KG, et al. 2015. Ultrafast polariton-phonon dynamics of strongly coupled quantum dot–nanocavity systems. *Phys. Rev. X* 5:031006
42. Laussy FP, del Valle E, Schrapp M, Laucht A, Finley JJ. 2012. Climbing the Jaynes–Cummings ladder by photon counting. *J. Nanophotonics* 6:061803

43. Deng H, Haug H, Yamamoto Y. 2010. Exciton-polariton Bose–Einstein condensation. *Rev. Mod. Phys.* 82:1489–537
44. Schwennicke K, Koner A, Perez-Sanchez JB, Xiong W, Giebink NC, et al. 2025. Unlocking delocalization: How much coupling strength is required to overcome energy disorder in molecular polaritons? *Chem. Sci.* 16:4676
45. del Pino J, Feist J, García-Vidal FJ. 2015. Quantum theory of collective strong coupling of molecular vibrations with a microcavity mode. *New J. Phys.* 17:053040
46. Thomas A, Jayachandran A, Lethuillier-Karl L, Vergauwe RM, Nagarajan K, et al. 2020. Ground state chemistry under vibrational strong coupling: dependence of thermodynamic parameters on the Rabi splitting energy. *Nanophotonics* 9:249–55
47. Campos-Gonzalez-Angulo JA, Poh YR, Du M, Yuen-Zhou J. 2023. Swinging between shine and shadow: theoretical advances on thermally activated vibropolaritonic chemistry. *J. Chem. Phys.* 158:230901
48. Simpkins BS, Dunkelberger AD, Vurgaftman I. 2023. Control, modulation, and analytical descriptions of vibrational strong coupling. *Chem. Rev.* 123:5020–48
49. Tavis M, Cummings FW. 1968. Exact solution for an *N*-molecule-radiation-field Hamiltonian. *Phys. Rev.* 170:379–84
50. Tavis M, Cummings FW. 1969. Approximate solutions for an *N*-molecule-radiation-field Hamiltonian. *Phys. Rev.* 188:692–95
51. Herrera F, Spano FC. 2016. Cavity-controlled chemistry in molecular ensembles. *Phys. Rev. Lett.* 116:238301
52. Herrera F, Spano FC. 2018. Theory of nanoscale organic cavities: the essential role of vibration-photon dressed states. *ACS Photonics* 5:65–79
53. Zeb MA, Kirton PG, Keeling J. 2018. Exact states and spectra of vibrationally dressed polaritons. *ACS Photonics* 5:249–57
54. Herrera F, Spano FC. 2017. Absorption and photoluminescence in organic cavity QED. *Phys. Rev. A* 95:053867
55. Arnardottir KB, Moilanen AJ, Strashko A, Törmä P, Keeling J. 2020. Multimode organic polariton lasing. *Phys. Rev. Lett.* 125:233603
56. Keeling J, Kéna-Cohen S. 2020. Bose–Einstein condensation of exciton-polaritons in organic microcavities. *Annu. Rev. Phys. Chem.* 71:435–59
57. Caldeira A, Leggett A. 1983. Quantum tunnelling in a dissipative system. *Ann. Phys.* 149:374–456
58. Lee MK, Huo P, Coker DF. 2016. Semiclassical path integral dynamics: photosynthetic energy transfer with realistic environment interactions. *Annu. Rev. Phys. Chem.* 67:639–68
59. Dutra S, Nienhuis G. 2000. Quantized mode of a leaky cavity. *Phys. Rev. A* 62:063805
60. Dutra S, Nienhuis G. 2000. Derivation of a Hamiltonian for photon decay in a cavity. *J. Opt. B* 2:584–88
61. Dutra SM. 2005. *Cavity Quantum Electrodynamics: The Strange Theory of Light in a Box*. John Wiley & Sons
62. Koessler ER, Mandal A, Huo P. 2022. Incorporating Lindblad decay dynamics into mixed quantum-classical simulations. *J. Chem. Phys.* 157:064101
63. Hopfield J. 1958. Theory of the contribution of excitons to the complex dielectric constant of crystals. *Phys. Rev.* 112:1555–67
64. Li TE, Nitzan A, Subotnik JE. 2022. Polariton relaxation under vibrational strong coupling: comparing cavity molecular dynamics simulations against Fermi's golden rule rate. *J. Chem. Phys.* 156:134106
65. Lai Y, Ying W, Huo P. 2024. Non-equilibrium rate theory for polariton relaxation dynamics. *J. Chem. Phys.* 161:104109
66. Ying W, Mondal ME, Huo P. 2024. Theory and quantum dynamics simulations of exciton-polariton motional narrowing. *J. Chem. Phys.* 161:064105
67. Mandal A, Montillo Vega S, Huo P. 2020. Polarized Fock states and the dynamical Casimir effect in molecular cavity quantum electrodynamics. *J. Phys. Chem. Lett.* 11:9215–23
68. Zhou W, Hu D, Mandal A, Huo P. 2022. Nuclear gradient expressions for molecular cavity quantum electrodynamics simulations using mixed quantum-classical methods. *J. Chem. Phys.* 157:104118
69. Hu D, Mandal A, Weight BM, Huo P. 2022. Quasi-diabatic propagation scheme for simulating polariton chemistry. *J. Chem. Phys.* 157:194109

70. Hu D, Huo P. 2023. Ab initio molecular cavity quantum electrodynamics simulations using machine learning models. *J. Chem. Theory Comput.* 19:2353–68
71. Takahashi S, Watanabe K. 2020. Decoupling from a thermal bath via molecular polariton formation. *J. Phys. Chem. Lett.* 11:1349–56
72. Nitzan A. 2006. *Chemical Dynamics in Condensed Phases: Relaxation, Transfer and Reactions in Condensed Molecular Systems*. Oxford Graduate Texts
73. Schwartz T, Hutchison JA, Léonard J, Genet C, Haacke S, Ebbesen TW. 2013. Polariton dynamics under strong light–molecule coupling. *ChemPhysChem* 14:125–31
74. Canaguier-Durand A, Genet C, Lambrecht A, Ebbesen TW, Reynaud S. 2015. Non-Markovian polariton dynamics in organic strong coupling. *Eur. Phys. J. D* 69:24
75. Mony J, Hertzog M, Kushwaha K, Börjesson K. 2018. Angle-independent polariton emission lifetime shown by perylene hybridized to the vacuum field inside a Fabry–Pérot cavity. *J. Phys. Chem. C* 122:24917–23
76. Xiang B, Ribeiro RF, Chen L, Wang J, Du M, et al. 2019. State-selective polariton to dark state relaxation dynamics. *J. Phys. Chem. A* 123:5918–27
77. Avramenko AG, Rury AS. 2020. Quantum control of ultrafast internal conversion using nanoconfined virtual photons. *J. Phys. Chem. Lett.* 11:1013–21
78. Laitz M, Kaplan AEK, Deschamps J, Barotov U, Proppe AH, et al. 2023. Uncovering temperature-dependent exciton-polariton relaxation mechanisms in hybrid organic-inorganic perovskites. *Nat. Commun.* 14:2426
79. Whittaker DM, Kinsler P, Fisher TA, Skolnick MS, Armitage A, et al. 1996. Motional narrowing in semiconductor microcavities. *Phys. Rev. Lett.* 77:4792–95
80. Wanasinghe ST, Gjoni A, Burson W, Majeski C, Zaslona B, Rury AS. 2024. Motional narrowing through photonic exchange: rational suppression of excitonic disorder from molecular cavity polariton formation. *J. Phys. Chem. Lett.* 15:2405–18
81. Odewale EO, Wanasinghe ST, Rury AS. 2024. Assessing the determinants of cavity polariton relaxation using angle-resolved photoluminescence excitation spectroscopy. *J. Phys. Chem. Lett.* 15:5705–13
82. del Pino J, Schröder FAYN, Chin AW, Feist J, García-Vidal FJ. 2018. Tensor network simulation of non-Markovian dynamics in organic polaritons. *Phys. Rev. Lett.* 121:227401
83. del Pino J, Schröder FAYN, Chin AW, Feist J, García-Vidal FJ. 2018. Tensor network simulation of polaron-polaritons in organic microcavities. *Phys. Rev. B* 98:165416
84. Sun K, Dou C, Gelin MF, Zhao Y. 2022. Dynamics of disordered Tavis–Cummings and Holstein–Tavis–Cummings models. *J. Chem. Phys.* 156:024102
85. Hou E, Sun K, Gelin MF, Zhao Y. 2024. Finite temperature dynamics of the Holstein–Tavis–Cummings model. *J. Chem. Phys.* 160:084116
86. Hu D, Chng BXK, Ying W, Huo P. 2025. Trajectory-based non-adiabatic simulations of the polariton relaxation dynamics. *J. Chem. Phys.* 162:124113
87. Mondal ME, Vamivakas AN, Cundiff ST, Krauss TD, Huo P. 2025. Polariton spectra under the collective coupling regime. I. Efficient simulation of linear spectra and quantum dynamics. *J. Chem. Phys.* 162:014114
88. Fowler-Wright P, Lovett BW, Keeling J. 2022. Efficient many-body non-Markovian dynamics of organic polaritons. *Phys. Rev. Lett.* 129:173001
89. Lindoy LP, Mandal A, Reichman DR. 2024. Investigating the collective nature of cavity-modified chemical kinetics under vibrational strong coupling. *Nanophotonics* 13:2617–33
90. Pérez-Sánchez JB, Koner A, Stern NP, Yuen-Zhou J. 2023. Simulating molecular polaritons in the collective regime using few-molecule models. *PNAS* 120:e2219223120
91. Pérez-Sánchez JB, Koner A, Raghavan-Chitra S, Yuen-Zhou J. 2025. CUT-E as a 1/*N* expansion for multiscale molecular polariton dynamics. *J. Chem. Phys.* 162:064101
92. Chng BXK, Ying W, Lai Y, Vamivakas AN, Cundiff ST, et al. 2024. Mechanism of molecular polariton decoherence in the collective light–matter couplings regime. *J. Phys. Chem. Lett.* 15:11773–83
93. Scholes GD, DelPo CA, Kudisch B. 2020. Entropy reorders polariton states. *J. Phys. Chem. Lett.* 11:6389–95

94. Wu N, Feist J, García-Vidal FJ. 2016. When polarons meet polaritons: exciton-vibration interactions in organic molecules strongly coupled to confined light fields. *Phys. Rev. B* 94:195409
95. Scholes GD. 2020. Polaritons and excitons: Hamiltonian design for enhanced coherence. *Proc. Math. Phys. Eng. Sci.* 476:20200278
96. Mondal ME, Koessler ER, Provazza J, Vamivakas AN, Cundiff ST, et al. 2023. Quantum dynamics simulations of the 2D spectroscopy for exciton polaritons. *J. Chem. Phys.* 159:094102
97. Mondal ME, Vamivakas AN, Cundiff ST, Krauss TD, Huo P. 2025. Polariton spectra under the collective coupling regime. II. 2D non-linear spectra. *J. Chem. Phys.* 162:074110
98. Timmer D, Gittinger M, Quenzel T, Stephan S, Zhang Y, et al. 2023. Plasmon mediated coherent population oscillations in molecular aggregates. *Nat. Commun.* 14:8035
99. Mukamel S. 1995. *Principles of Nonlinear Optical Spectroscopy*. Oxford University Press
100. Yuen-Zhou J, Koner A. 2024. Linear response of molecular polaritons. *J. Chem. Phys.* 160:154107
101. Schwennicke K, Koner A, Perez-Sanchez JB, Xiong W, Giebink NC, et al. 2025. When do molecular polaritons behave like optical filters? *Chem. Soc. Rev.* 54:6482–504
102. Litinskaia M, Kaganova I. 2000. Motional narrowing in a microcavity: contribution to the lower polariton linewidth. *Phys. Lett. A* 275:292–98
103. Savona V, Piermarocchi C, Quattropani A, Tassone F, Schwendimann P. 1997. Microscopic theory of motional narrowing of microcavity polaritons in a disordered potential. *Phys. Rev. Lett.* 78:4470–73
104. Whittaker DM. 1998. What determines inhomogeneous linewidths in semiconductor microcavities? *Phys. Rev. Lett.* 80:4791–94
105. Neuman T, Aizpurua J. 2018. Origin of the asymmetric light emission from molecular exciton–polaritons. *Optica* 5:1247
106. Thomas PA, Tan WJ, Kravets VG, Grigorenko AN, Barnes WL. 2024. Non-polaritonic effects in cavity-modified photochemistry. *Adv. Mater.* 36:2309393
107. Schwartz T, Hutchison JA. 2024. On the importance of experimental details: a comment on "Non-Polaritonic Effects in Cavity-Modified Photochemistry". Preprint, arXiv:2403.06001v1 [physics.chem-ph]
108. Koessler ER, Mandal A, Musser AJ, Krauss TD, Huo P. 2025. Polariton mediated electron transfer under the collective molecule–cavity coupling regime. *Chem. Sci.* 16:11644–58
109. Mauro L, Caicedo K, Jonusauskas G, Avriller R. 2021. Charge-transfer chemical reactions in nanofluidic Fabry–Pérot cavities. *Phys. Rev. B* 103:165412
110. Phuc NT. 2021. Super-reaction: the collective enhancement of a reaction rate by molecular polaritons in the presence of energy fluctuations. *J. Chem. Phys.* 155:014308
111. Sharma SK, Chen HT. 2024. Unraveling abnormal collective effects via the non-monotonic number dependence of electron transfer in confined electromagnetic fields. *J. Chem. Phys.* 161:104102
112. Eizner E, Martínez-Martínez LA, Yuen-Zhou J, Kéna-Cohen S. 2019. Inverting singlet and triplet excited states using strong light–matter coupling. *Sci. Adv.* 5:eaax4482
113. Sau A, Nagarajan K, Patrahau B, Lethuillier-Karl L, Vergauwe RMA, et al. 2021. Modifying Woodward–Hoffmann stereoselectivity under vibrational strong coupling. *Angew. Chem. Int. Ed.* 60:5712–17
114. Lather J, Thabassum ANK, Singh J, George J. 2022. Cavity catalysis: modifying linear free-energy relationship under cooperative vibrational strong coupling. *Chem. Sci.* 13:195–202
115. Hirai K, Takeda R, Hutchison JA, Uji-i H. 2020. Modulation of Prins cyclization by vibrational strong coupling. *Angew. Chem. Int. Ed.* 59:5332–35
116. Verdelli F, Wei YC, Joseph K, Abdelkhalik MS, Goudarzi M, et al. 2024. Polaritonic chemistry enabled by non-local metasurfaces. *Angew. Chem. Int. Ed.* 63:e202409528
117. Li TE, Nitzan A, Subotnik JE. 2020. On the origin of ground-state vacuum-field catalysis: equilibrium consideration. *J. Chem. Phys.* 152:234107
118. Campos-Gonzalez-Angulo JA, Yuen-Zhou J. 2020. Polaritonic normal modes in transition state theory. *J. Chem. Phys.* 152:161101
119. Schäfer C, Flick J, Ronca E, Narang P, Rubio A. 2021. Shining light on the microscopic resonant mechanism responsible for cavity-mediated chemical reactivity. *Nat. Commun.* 13:7817
120. Li X, Mandal A, Huo P. 2021. Cavity frequency–dependent theory for vibrational polariton chemistry. *Nat. Commun.* 12:1315

121. Lindoy LP, Mandal A, Reichman DR. 2022. Resonant cavity modification of ground-state chemical kinetics. *J. Phys. Chem. Lett.* 13:6580–86
122. Wang DS, Neuman T, Yelin SF, Flick J. 2022. Cavity-modified unimolecular dissociation reactions via intramolecular vibrational energy redistribution. *J. Phys. Chem. Lett.* 13:3317–24
123. Du M, Poh YR, Yuen-Zhou J. 2023. Vibropolaritonic reaction rates in the collective strong coupling regime: Pollak–Grabert–Hänggi theory. *J. Phys. Chem. C* 127:5230–37
124. Mandal A, Li X, Huo P. 2022. Theory of vibrational polariton chemistry in the collective coupling regime. *J. Chem. Phys.* 156:014101
125. Yang PY, Cao J. 2021. Quantum effects in chemical reactions under polaritonic vibrational strong coupling. *J. Phys. Chem. Lett.* 12:9531–38
126. Sun J, Vendrell O. 2022. Suppression and enhancement of thermal chemical rates in a cavity. *J. Phys. Chem. Lett.* 13:4441–46
127. Fiechter MR, Runeson JE, Lawrence JE, Richardson JO. 2023. How quantum is the resonance behavior in vibrational polariton chemistry? *J. Phys. Chem. Lett.* 14:8261–67
128. Anderson MC, Woods EJ, Fay TP, Wales DJ, Limmer DT. 2023. On the mechanism of polaritonic rate suppression from quantum transition paths. *J. Phys. Chem. Lett.* 14:6888–94
129. Lindoy LP, Mandal A, Reichman DR. 2023. Quantum dynamical effects of vibrational strong coupling in chemical reactivity. *Nat. Commun.* 14:2733
130. Ying W, Huo P. 2023. Resonance theory and quantum dynamics simulations of vibrational polariton chemistry. *J. Chem. Phys.* 159:084104
131. Hu D, Ying W, Huo P. 2023. Resonance enhancement of vibrational polariton chemistry obtained from the mixed quantum-classical dynamics simulations. *J. Phys. Chem. Lett.* 14:11208–16
132. Ke Y, Richardson JO. 2024. Insights into the mechanisms of optical cavity–modified ground-state chemical reactions. *J. Chem. Phys.* 160:224704
133. Ke Y, Richardson JO. 2024. Quantum nature of reactivity modification in vibrational polariton chemistry. *J. Chem. Phys.* 161:054104
134. Ying W, Huo P. 2024. Resonance theory of vibrational strong coupling enhanced polariton chemistry and the role of photonic mode lifetime. *Commun. Mater.* 5:110
135. Ying W, Taylor MAD, Huo P. 2024. Resonance theory of vibrational polariton chemistry at the normal incidence. *Nanophotonics* 13:2601–15
136. Vega SM, Ying W, Huo P. 2025. Theoretical insights into the resonant suppression effect in vibrational polariton chemistry. *J. Am. Chem. Soc.* 147:19727–37
137. Li TE, Nitzan A, Subotnik JE. 2021. Collective vibrational strong coupling effects on molecular vibrational relaxation and energy transfer: numerical insights via cavity molecular dynamics simulations. *Angew. Chem. Int. Ed.* 60:15533–40
138. Shalabney A, George J, Hutchison J, Pupillo G, Genet C, Ebbesen TW. 2015. Coherent coupling of molecular resonators with a microcavity mode. *Nat. Commun.* 6:5981
139. Kramers HA, Heisenberg W. 1925. Über die Streuung von Strahlung durch Atome. *Z. Phys.* 31:681–708
140. Hänggi P, Talkner P, Borkovec M. 1990. Reaction-rate theory: fifty years after Kramers. *Rev. Mod. Phys.* 62:251–341
141. Fidler AP, Chen L, McKillop AM, Weichman ML. 2023. Ultrafast dynamics of CN radical reactions with chloroform solvent under vibrational strong coupling. *J. Chem. Phys.* 159:164302
142. Chen L, Fidler AP, McKillop AM, Weichman ML. 2024. Exploring the impact of vibrational cavity coupling strength on ultrafast CN + c-C_6H_{12} reaction dynamics. *Nanophotonics* 13:2591–99
143. Hirai K, Hutchison JA, Uji-i H. 2020. Recent progress in vibropolaritonic chemistry. *ChemPlusChem* 85:1981–88